J. Fluid Mech. (2018), *vol.* 835, *pp.* 217–251. © Cambridge University Press 2017
doi:10.1017/jfm.2017.742

Turbulent boundary layers absent mean shear

Blair A. Johnson[1,†] **and Edwin A. Cowen**[2]

[1]Department of Civil, Architectural and Environmental Engineering, The University of Texas at Austin, Austin, TX 78712, USA

[2]DeFrees Hydraulics Laboratory, School of Civil and Environmental Engineering, Cornell University, Ithaca, NY 14853, USA

(Received 29 December 2016; revised 4 October 2017; accepted 11 October 2017; first published online 27 November 2017)

We perform an experimental study to investigate the turbulent boundary layer above a stationary solid glass bed in the absence of mean shear. High Reynolds number ($Re_\lambda \sim 300$) horizontally homogeneous isotropic turbulence is generated via randomly actuated synthetic jet arrays (RASJA – Variano & Cowen *J. Fluid Mech.* vol. 604, 2008, pp. 1–32). Each of the arrays is controlled by a spatio-temporally varying algorithm, which in turn minimizes the formation of secondary mean flows. One array consists of an 8×8 grid of jets, while the other is a 16×16 array. Particle image velocimetry measurements are used to study the isotropic turbulent region and the boundary layer formed beneath as the turbulence encounters a stationary wall. The flow is characterized with statistical metrics including the mean flow and turbulent velocities, turbulent kinetic energy, integral scales and the turbulent kinetic energy transport equation, which includes the energy dissipation rate, production and turbulent transport. The empirical constant in the Tennekes (*J. Fluid Mech.* vol. 67, 1975, pp. 561–567) model of Eulerian frequency spectra is calculated based on the dissipation results and temporal frequency spectra from acoustic Doppler velocimetry measurements. We compare our results to prior literature that addresses mean shear free turbulent boundary layer characterizations via grid-stirred tank experiments, moving-bed experiments, rapid-distortion theory and direct numerical simulations in a forced turbulent box. By varying the operational parameters of the randomly actuated synthetic jet array, we also find that we are able to control the turbulence levels, including integral length scales and dissipation rates, by changing the mean on-times in the jet algorithm.

Key words: homogeneous turbulence, isotropic turbulence, turbulent boundary layers

1. Introduction

Classic shear-driven turbulent boundary layers have been studied extensively, dating back to the canonical work of von Kármán (1930), who presented significant contributions to boundary layer characterizations that are still used today. Such boundary layers are well understood, and there is a breadth of literature describing ways in which the viscous interaction between the mean flow and under- or overlying

† Email address for correspondence: blairjohnson@utexas.edu

interface can generate substantial shear stress, turbulence and transport, depending on the flow and boundary characteristics. A boundary layer is a region where flow is affected by the presence of a boundary, and it is necessarily overlain by a region of the flow that is unaffected by the presence of a boundary. However, mean shear is not a requisite component of a boundary layer. While boundary layers formed as a result of mean shear are of obvious importance in environmental and industrial flows, relatively little is known of boundary layers in which turbulence is dominant and mean shear is minimal.

When turbulence levels are in excess of those that are generated by wall-bounded mean shear stress, for example, in bore-advected turbulence in coastal zones (Cowen *et al.* 2003), the boundary layers vary greatly with respect to classic shear-driven models. In contrast to shear-driven flows, it is possible for turbulence levels to be set by offshore wave activity or by interactions of wakes passing through vegetation, for example. The boundary layers formed in cases such as these interact quite differently with surrounding interfaces, whether free slip, solid, mobile, porous or other. Additionally, it becomes non-trivial to understand interfacial shear stress in these flows, as we must reconsider what generates stress on a boundary with active turbulence but little or no mean shear. For example, to date there are no satisfactory models to predict incipient sediment motion by shear generated due to turbulence alone.

A variety of studies have been performed to address turbulence in the absence of mean shear via two main turbulence generation models: turbulent boxes and moving beds. Experimentally, the former primarily encompasses grid-stirred tanks (GSTs), in which interacting wakes from an oscillating grid stir ambient fluid into homogeneous isotropic turbulent flow away from the grid. In numerical models, this is typically achieved by inserting an interface, whether via a solid wall or non-turbulent fluid, into a shear free turbulent flow. Moving-bed experiments are characterized by the advection of grid-generated turbulence over a boundary moved at the mean flow speed in order to eliminate mean boundary shear.

GSTs were initially developed to investigate mixing and entrainment rates in low mean flow environments (Rouse & Dodu 1955). Without additional flow forcing or damping mechanisms present in GSTs, it was generally assumed that mean flows were not present, and thus, the GST became popular for studying mean shear free turbulent boundary layers throughout the latter half of the twentieth century. Early studies explored the dependence of root mean square (r.m.s.) velocities and turbulent kinetic energy upon grid characteristics and the parameters prescribing the grid's motion. The dependence was studied as a function of the mesh size of the grid, as well as the driving amplitude and frequency of the oscillations. Away from boundaries, r.m.s. velocities were found to decay with distance from the grid throughout the tank as αz^{-1} (Thompson & Turner 1975, among others). Hopfinger & Toly (1976) found the relationship $u' = 0.25fS^{1.5}J^{0.5}z^{-1}$ to characterize the strength of boundary-parallel r.m.s. velocity fluctuations, where f, S and J, the frequency, stroke and mesh spacing, respectively, are all fixed parameters of the grid. This leads to a continuous decay in both boundary-normal and boundary-parallel r.m.s. velocities with distance from the turbulence generating mechanism.

GSTs have also been used to study turbulent boundary layers absent mean shear at free surfaces by, *inter alia*, Brumley & Jirka (1987), who found the depth of the surface-influenced layer to scale with the integral length scale, whereas the turbulence of the surface-influenced layer scales with depth and with dissipation. They also observed an increase in wall-parallel r.m.s. velocities at the free surface that is not

predicted by decay relationships of Hopfinger & Toly (1976). Interestingly, GSTs have not been used to characterize turbulent boundary layers absent mean shear at a solid boundary.

Despite widespread usage of GSTs and accompanying assumptions of negligible mean flow, several experimentalists questioned their reliability and have since observed significant secondary motions (e.g. Hopfinger & Toly 1976; McDougall 1979). McKenna & McGillis (2004) found that the mean flow strength, or the ratio of mean velocities to r.m.s. velocities, was commonly as high as 25 %, and that the presence of mean secondary circulations is inherent to GSTs, due to the spatially symmetric forcing of the oscillating grids.

Motivated by an interest in generating highly turbulent flows absent mean shear, Variano, Bodenschatz & Cowen (2004) developed a facility with a spatio-temporally varying randomly actuated synthetic jet array (RASJA) that generates highly energetic turbulence with reduced secondary flows relative to what is commonly observed in GSTs. Studies have been performed to research the effect of the spatial layout of the jets on turbulence generated away from the source, and it was shown that a random algorithm without spatially correlated jet firing produced highly turbulent flows with negligible mean flows (Perez-Alvarado, Mydlarski & Gaskin 2016). Random jet arrays have been used to study mean shear free turbulence at a free surface (Variano & Cowen 2008, 2013) but not at a solid boundary. This is our method of choice for generating turbulent boundary layers and it is summarized in § 2.

Moving-bed experiments were first performed by Uzkan & Reynolds (1967) and Thomas & Hancock (1977) in water and air, respectively. While the former found damping of turbulence at the wall that scaled with a viscous length scale, the latter observed an increase in turbulence at the moving wall, due to kinematic 'blocking' effects that increase wall-parallel r.m.s. velocities (Perot & Moin 1995*a*). Hunt & Graham (1978) used rapid-distortion theory (RDT) to explore these particular flows. They defined regions of the boundary layer, including an outer 'source region', the thickness of which scales with the integral length scale of the turbulence, and an inner 'viscous region' that is dependent upon the free stream flow velocity and distance downstream, although much of the boundary layer theory developed is for the inviscid case. This was extended by Hunt (1984) to account for nonlinear effects that can develop in the boundary layer and who also explored wall-normal velocity fluctuations and dissipation more thoroughly.

Teixeira & Belcher (2000) extended the RDT analysis of Hunt & Graham (1978) to account for viscosity and to include dissipation estimates at both a solid wall and free surface by inserting a flat plate boundary into stationary turbulence. Their findings of increased wall-parallel r.m.s. velocities and dissipation rates due to the viscous no-slip condition at a solid wall agree well with the direct numerical simulations (DNS) of Perot & Moin (1995*a*,*b*) that investigated intercomponent energy transfer, Reynolds stresses and dissipation rates at a stationary permeable wall, free surface and solid wall. Teixeira & Belcher (2000) observed enhanced dissipation of bed-parallel r.m.s. velocities at a solid wall; this is also shown in the RDT extension of Teixeira & da Silva (2012), who carefully examine near-bed contributions of dissipation from three-component velocity derivatives.

To better understand the role of turbulence in a mean shear free environment, we perform laboratory experiments in a facility designed to generate homogeneous isotropic turbulence in the absence of mean shear. We modified the facility introduced in Variano *et al.* (2004) by suspending the RASJA at the top of a water tank with downward-facing jets, whose wakes merge to stir the surrounding fluid into

horizontally homogeneous isotropic turbulence with negligible mean flow. We have also constructed an additional RASJA, increasing the number of jets from 64 in the original to 256 in the new array, with 4 times the density of jets. This allows more flexibility in the levels of turbulence generated and also produces a non-dimensionally deeper tank, with respect to the jet spacing of each array. This provides two jet spacings, analogous to changing J in a GST. The algorithm that controls the individual jet activity, termed the 'sunbathing' algorithm, is described in Variano & Cowen (2008) and it significantly reduces mean flows in comparison with GSTs as they demonstrate. We explore details of this algorithm that alter the development of turbulence in the facility, with particular focus on controlling the integral length scale with jet activity.

We perform experiments above a rigid impermeable glass plate. Through these experiments, we make comparisons between our facility and the aforementioned experimental and theoretical works involving grid-stirred tanks, moving beds and temporally evolving numerical turbulent/non-turbulent interfaces. Due to the different boundary conditions in each of these set-ups, we are uniquely positioned to evaluate the assumptions made in each prior facility given our experiments with a stationary bed and negligible secondary flows.

With data collected via acoustic Doppler velocimetry (ADV) and particle image velocimetry (PIV), we characterize flows in the tank, with emphasis on the region in which the flow is nearly isotropic and the near-bed region where assumptions of isotropy begin to break down, i.e. the boundary layer. We examine mean and secondary flows, r.m.s. velocities, turbulent kinetic energy, integral scales and spectra, and we explore the relationship between the sunbathing algorithm and these parameters. We evaluate the contributing terms in the turbulent kinetic energy balance including dissipation, production, turbulent transport and pressure diffusion to understand how this unique mean shear free boundary layer compares to traditional shear-driven boundary layers.

2. Experimental facility

2.1. *Apparatus*

Experiments are conducted in the DeFrees Hydraulics Laboratory at Cornell University in a 1.000 m tall tank with a 0.800 by 0.800 m horizontal cross-sectional area. Turbulence is generated by RASJAs suspended above the facility. A 1.27 cm thick glass plate is mounted into the bottom of the facility to provide a stable rigid bed. The top of the glass is located 8 cm above the base of the tank for adequate optical access.

The coordinate system is shown in figure 1, with $z = 0$ at the top of the bed increasing upwards to H, the height of the jet orifice plane relative to the bed. At the lateral centre of the facility, $x = 0$ and $y = 0$, each orthogonal to the side walls and following the right-hand rule. Velocity components U, V and W follow the x-, y- and z-directions, respectively.

2.1.1. *The* 8×8 *RASJA*

The original RASJA, pictured in figure 2, consists of 64 downward-facing jets arranged on an 8×8 square grid with a spacing, J, of 10.0 cm from jet orifice centre-to-centre. Each jet is generated by a 12 V 2.1 A Rule 360 g.p.h. bilge pump with a 2.19 cm diameter PVC elbow to direct the pump flow downward with an outlet velocity of 100 cm s^{-1}, as determined by the flow rate in the specifications

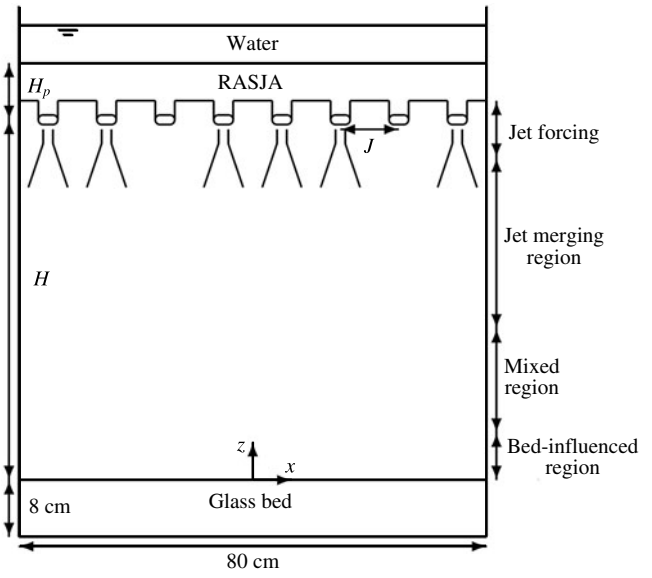

FIGURE 1. Schematic drawing of the turbulence facility with the 8×8 RASJA.

FIGURE 2. (Colour online) Photo of tank with the 8×8 RASJA.

and jet diameter. Each jet simultaneously intakes the same volume of water that it expels; thus, the jets are termed 'synthetic' in that they inject momentum, but no net

mass, into the flow. The jet Reynolds number of each individual jet is $Re_{jet} = 22\,000$, with 20 °C water to determine kinematic viscosity ν.

The jets are mounted to an acrylic support panel that has several holes for instrument access. The water is filled a minimum of 3 cm above the support panel. All experiments with the 8×8 RASJA reported herein were performed with the jet orifice plane at $H = 71.0$ cm above the bed, which is the maximum height to which the jets can be raised in this configuration. This is a sufficient height for the jet wakes to merge into homogeneous turbulence above the bed, as it was shown in Variano & Cowen (2008) and Perez-Alvarado *et al.* (2016) that mixing is achieved for $H/J > 6$. The pump intake plane is $H_p = 7.0$ cm above the orifice plane.

The on–off states of the jets are controlled in Mathworks MATLAB via a Measurement Computing 96-channel digital output card (PCI-DIO96H) that triggers solid-state relays to activate the pumps. The sunbathing algorithm is updated at a 10 Hz output frequency. The algorithm randomly selects instantaneous on-times from Gaussian distributions given user-input operation parameters T_{on}, the mean on-time of each jet and Φ_{on}, the mean percentage of jet activity. Φ_{on} is ultimately determined by the ratio of $T_{on}/T_{on} + T_{off}$, and standard deviations σ_{on} and σ_{off} are set to one third of the value of T_{on} and T_{off}, respectively, in the Gaussian distribution, with limits set to prevent negative on-times.

Variano & Cowen (2008) found maximum turbulent kinetic energy generation for $6 < \Phi_{on} < 25\,\%$ at $T_{on} = 3$ s. We explore controlling the turbulence levels by varying the sunbathing parameters through a total of 15 combinations for $\Phi_{on} = 6.25$, 7.7, 9.1, 10.5, 12.5 % and $T_{on} = 4$, 6, 8 s. Mean on-times longer than 8 s cause direct impingement of the jets onto the bed in this facility with the 8×8 RASJA, and on-times shorter than 4 s resulted in non-negligible secondary recirculations in this configuration. Because the levels of turbulent kinetic energy were found to be symmetric about $\Phi_{on} = 12.5\,\%$ in Variano & Cowen (2008), we opted to explore percentages lower than 12.5 % to prolong the life of the jets. Note that all 64 jets run during a 30 min test, even with low values of Φ_{on}. We have also added a jet-monitoring system to ensure optimal jet performance; additional details are presented in Johnson (2016).

2.1.2. *The* 16×16 *RASJA*

The new facility consists of 256 jets arranged on a square 16×16 grid with $J = 5.0$ cm. The jets are generated by 12 V 2.8 A Rule il200 submersible inline pumps. Each pump has a specified flow rate of 168 g.p.h. through an 8.0 mm downward nozzle. This produces an outlet velocity of 350 cm s^{-1} with a jet Reynolds number Re_{jet} of 28 000. The jets are suspended at $H = 65.0$ cm above the bed, resulting in a non-dimensional jet height $(H/J) = 13$, nearly twice the value obtained in the 8×8 RASJA. There is an intake plane $H_p = 12.9$ cm above the jet orifice plane. There is no lid on the facility, and the water is filled approximately 8 cm above the intake plane to ensure air does not enter the pumps. With a significant increase in Re_{jet} and an increase in the number of jets by a factor of 4 relative to the 8×8 RASJA, we explore much lower values of T_{on} and Φ_{on}, with 0.8 s $< T_{on} <$ 1.6 s and Φ_{on} of 3.1 %.

The 16×16 RASJA is controlled via a single Arduino Mega 2560 microcontroller. Instantaneous on–off states are selected from Gaussian distributions in MATLAB using the same sunbathing algorithm as with the 8×8 RASJA, and MATLAB transmits instantaneous on–off states to the Arduino through serial communication with an update frequency of 10 Hz. The Arduino microcontroller sends on–off signals to the 256 jets by passing 32 bytes to shift registers (Texas Instruments SN74HC595N) and integrated circuit driver arrays (MIC2981/82YN) on the pump control boards; 1 byte contains the on–off states of 8 individual jets.

2.2. *Measurement techniques*

ADV measurements are made using a Nortek Vectrino with 'plus' firmware to record three components of velocity at a single point location. All results shown herein are located 12.0 cm above the bed at the lateral centre of the tank, as shown in figure 2. The instrument is mounted vertically, with the z-axis of the ADV aligned with the z-axis of the tank, and the instrument x- and y-axes orthogonal to the tank walls. Measurements are recorded at a sampling frequency of 100 Hz with a sampling volume length of 7.0 mm and transmit length of 1.8 mm. To ensure convergence of turbulence statistics, data records are at least 30 min long. An adaptive Gaussian (AGW) filter (Cowen & Monismith 1997) is applied to eliminate spurious measurements due to instrument noise and/or instantaneously low seeding density. Less than 1 % of the data are eliminated through this method. Filtered data points are linearly interpolated to compute frequency spectra as they require a continuous temporal record.

Arkema Group ORGASOL (R) 2002 ES 3 Nat 3 Polyamide 12 nylon particles are used to seed the flow for accurate ADV measurements. These particles feature an average batch diameter $D_p = 29.4$ μm, with 5 % less than 20 μm and 8 % greater than 40 μm. With a specific gravity of 1.03, they are effectively neutrally buoyant. For all flow cases considered, the Stokes number $St = (\tau_R/\tau_\mu)$ in which τ_μ represents the Kolmogorov time scale (details presented in § 5.5) and $\tau_R = ((S)D_p^2/18\nu)$ is a relaxation time scale, we find values of St consistently less than 0.001. With $St \ll 1$, we conclude that the particles follow the flow as passive tracers.

PIV is used to record spatio-temporal data in the lateral centre of the tank, in the x–z plane, at the bottom boundary. Measurements are collected using an Imperx Bobcat IGV-2020 camera with 2056 by 2060 pixel resolution and either a Nikkor 50 mm lens or Nikon 60 mm lens, each with $f/2.8$. Illumination is provided by a Coherent Innova 90 Argon Ion laser operated at approximately 3 W power with wavelengths of 488 and 514.5 nm in multi-line mode. The beam, which is 1.4 mm in diameter, passes through a 2.5 mm mechanical shutter (NM technologies LS200) and is scanned through the planar field-of-view (FOV) with a mirror (Cambridge Technologies 6M8505X-V) attached to a galvanometer (Cambridge Technologies 6860). Each scan is completed within 5 ms, and the time, Δt, between the scans is 8 ms.

The shutter, mirror and camera are synchronized using a National Instruments analogue output card (PCI-6711) controlled by MATLAB. The same nylon ORGASOL particles are also used for PIV measurements, though PIV and ADV data are not collected simultaneously. Velocity fields are acquired at a sampling frequency f_s of 1 Hz to ensure uncorrelated samples. Results reported herein are for tests of 30 min in duration, which was found to be a sufficient period of time for statistics to converge to the same levels as if tests were run over a 24 h period (Variano & Cowen 2008).

Image analysis is performed in MATLAB using a sub-pixel cross-correlation peak locating PIV algorithm developed by Liao & Cowen (2005) and based on Cowen & Monismith (1997). This accurately determines particle displacements between image pairs separated by a time Δt, with a spectral continuous subwindow shifting method to improve subpixel particle displacements. In order to reduce error caused by tracer particles that are highly sheared due to the energy of the turbulent flow, we artificially expand the illuminated tracer particles by convolving the images with a 4×4 Gaussian kernel using MATLAB's `imfilter` function, as is described in Variano (2007).

Before analysing the images, we perform pre-processing to remove background noise introduced by uniform ambient light and reflections off of the glass bed. As in

Cowen & Monismith (1997), we look temporally across all pixels in the first image of every pair and compute the minimum light intensity to compile a single background image. We repeat this process to compute a background image for all of the second images. These background images are subtracted from all of the raw images.

An initial interrogation is completed with 64×64 pixel subwindows with 50 % overlap in order to determine a first estimate for particle displacements across the FOV. There are 6 iterations for the algorithm to converge upon pixel displacements in each subwindow. The resulting converged vectors from the initial pass are smoothed according to the median of valid vectors within a 3×3 array of neighbouring subwindows. The results of the median filter smoothing of valid particle displacements are then used to guide a more refined grid with 32×32 pixel subwindow interrogation of the images, again with 50 % overlap, to obtain the final particle displacements. The resulting spatial resolution for the experiments presented herein is 1.76 mm from subwindow centre-to-centre with an approximately 20×20 cm FOV, depending on the precise location of the camera.

Several post-processing filters are applied to reduce spurious velocity vectors from the measurements. First, unconverged vectors are removed. An AGW filter is then applied to remove the uniformly distributed spurious vectors that lie outside the statistical bounds of the assumed Gaussian distributed turbulence measurements. This is performed across all time at given subwindow heights above the bed. Finally, a 5×5 local median filter, with a threshold determined by the user (Westerweel 1994; Cowen & Monismith 1997) is applied to remove spurious data within an instantaneous image that lie within the statistical bounds of the assumed Gaussian distributed turbulence measurements. Between 80 and 97 % of data are declared valid, with regions of high shear contributing to fewer valid vectors. Removed data are not replaced through interpolation, as interpolation can significantly alter resulting statistical analyses.

Velocity data are Reynolds decomposed such that $U(x, y, z, t) = \langle U(x, y, z)\rangle + u(x, y, z, t)$ and likewise for V and W. The angle brackets denote a temporal average and lower case letters represent fluctuations. According to ADV data, the flow is radially symmetric about the z-axis (see Johnson (2016) for details), thus we only report statistics along the x–z plane. Lateral variations across the 20 cm FOV are sufficiently small to allow us to invoke horizontal homogeneity. We use an overbar to indicate averages that include time and space (i.e. the horizontal average of $\langle U\rangle$ is $\overline{U}$).

We use the bootstrap method (Efron & Tibshirani 1993) to construct 95 % confidence intervals of the turbulence statistics to compute uncertainty bounds. With our assumptions of convergence and horizontal homogeneity, the bootstrap analyses presented typically utilize between 1800 and 225 000 data points, resampled 1000 times, with replacement, to generate ordered random samples. The 95 % confidence interval is determined by the 97.5 percentile and 2.5 percentile statistic.

3. Exploration of the RASJA algorithm

We first aim to characterize flows in this unique facility by exploring metrics such as mean velocities, turbulent velocity fluctuations, and secondary flows. This allows us to see how the flow varies with distance from the jets and proximity to the bed. It also provides a first-order understanding of the energetics of the turbulence and the relative strength of mean flows to turbulent velocity fluctuations.

We also explore the effect of altering the sunbathing parameters T_{on} and Φ_{on} on the turbulence generated in order to complement the growing field of experimental

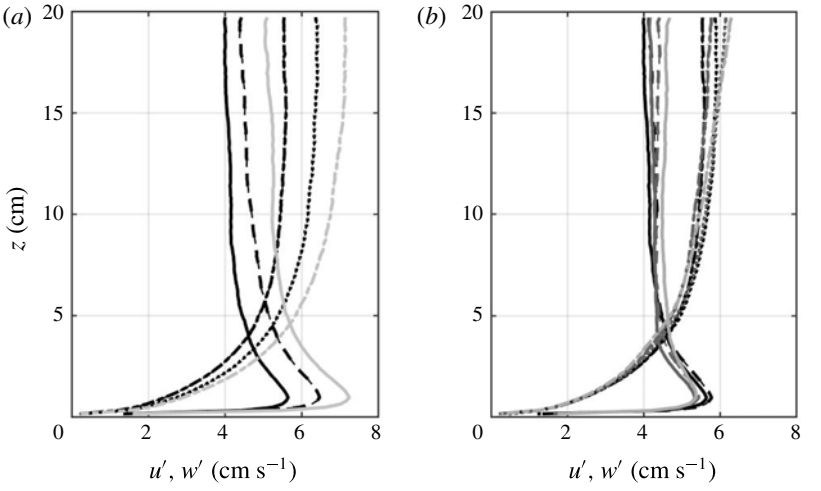

FIGURE 3. Dependence of u' and w' on $T_{on} = 4$ s ($u' = -$, $w' = -\cdot$), 6 s ($u' = --$, $w' = \cdots$), 8 s ($u' = -$ (grey), $w' = -\cdot$ (grey)) for $\Phi_{on} = 6.25\,\%$ (*a*) and $\Phi_{on} = 6.25\,\%$ ($u' = -$, $w' = -\cdot$), 7.7 % ($u' = --$, $w' = \cdots$), 9.1 % ($u' = -$ (grey), $w' = -\cdot$ (grey)), 10.5 % ($u' = --$ (grey), $w' = \cdots$ (grey)), 12.5 % ($u' = -$ (grey), $w' = -\cdot$ (grey)) for $T_{on} = 4$ s (*b*). 8×8 RASJA.

turbulence generation and interest in random jet arrays. Because the integral length scale of turbulence is typically thought to depend on the geometry of an experimental facility, we specifically consider whether we can control the integral length scale by varying T_{on} within each facility, which is analogous to changing the stroke (S) of GSTs, and varying J between facilities.

3.1. *Mean and fluctuating velocities*

As expected, temporally averaged flow fields show near-zero mean velocity profiles for both RASJAs. Of the 15 experimental cases considered with the 8×8 RASJA, we find typical mean horizontal velocities with magnitudes of approximately 0.15 cm s^{-1}. The vertical forcing of the jets induces a weak mean decaying downward flow in the centre of the tank, with return flows at the walls. Typical values of these downward velocities are approximately 0.47 cm s^{-1} in the mixed region of the facility (i.e. the region below which the jet wakes have merged and above which the flow is affected by the presence of the boundary). These velocities are low relative to the velocity fluctuations, as is presented in § 3.2.

We define the bed-normal r.m.s. velocity as $u' = \sqrt{\overline{u^2}}$ (and likewise for v' and w') to consider the strength of the turbulent velocity fluctuations. Figure 3 explores the influence of T_{on} (left) and Φ_{on} (right) on u' and w' for the 8×8 RASJA. While Φ_{on} has a relatively negligible impact on u' and w', we observe a strong dependence upon T_{on}. As subsequent statistical analyses also show a greater dependence upon T_{on} rather than Φ_{on}, we present the remaining statistical analyses controlled only by varying T_{on} for a selected Φ_{on} of 6.25 %.

Given the relative independence of the turbulent velocity fluctuations on Φ_{on} observed with the 8×8 RASJA, we select a single Φ_{on} of 3.1 % with which to perform 5 tests on the 16×16 RASJA with varying T_{on}. Results from these experiments are summarized in figure 4. Similar trends are observed between the

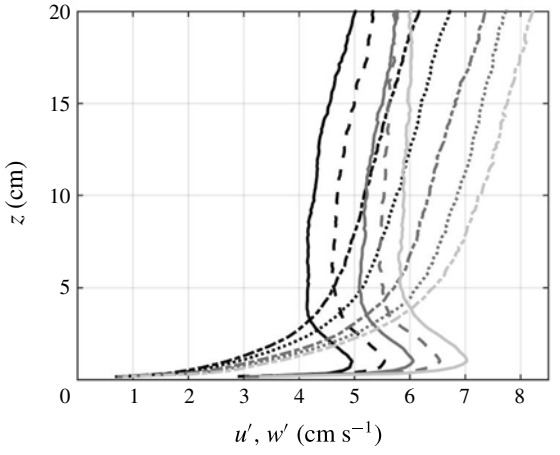

FIGURE 4. Dependence of u' and w' on $T_{on} = 0.8$ s ($u' = -$, $w' = -\cdot$), 1.0 s ($u' = --$, $w' = \cdots$), 1.2 s ($u' = -$ (grey), $w' = -\cdot$ (grey)), 1.4 s ($u' = --$ (grey), $w' = \cdots$ (grey)) 1.6 s ($u' = -$ (light grey), $w' = -\cdot$ (light grey)). $\Phi_{on} = 3.1\,\%$, 16×16 RASJA.

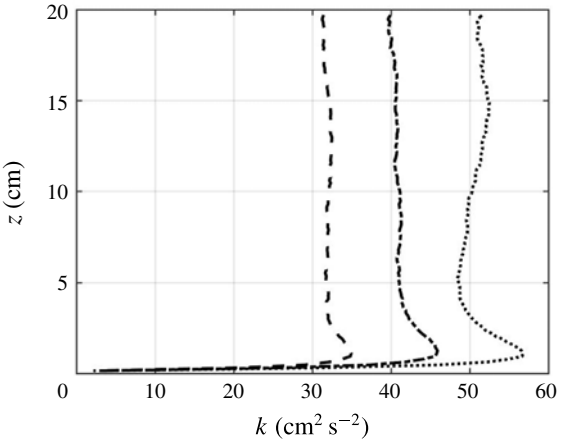

FIGURE 5. Turbulent kinetic energy profiles for $\Phi_{on} = 6.25\,\%$, $T_{on} = 4$ s ($--$), 6 s ($-\cdot$), 8 s ($\cdots$). 8×8 RASJA.

8×8 and 16×16 RASJAs, with a clear relationship between the r.m.s. velocities and T_{on}. Because the r.m.s. velocities are similar in magnitude in the 8×8 RASJA trial for $\Phi_{on} = 6.25\,\%$, $T_{on} = 4$ s and the 16×16 RASJA trial for $\Phi_{on} = 3.1\,\%$, $T_{on} = 0.8$ s, we use these two cases for several sample plots in the remainder of this article to draw comparisons.

3.2. *Turbulent kinetic energy and secondary flows*

We compute turbulent kinetic energy, k, from PIV data as $k = 1/2(2u'^2 + w'^2)$ by invoking radial symmetry. As expected from the r.m.s. velocity results, k increases with T_{on} in the turbulence facility using either the 8×8 RASJA or the 16×16 RASJA, as shown in figures 5 and 6, respectively.

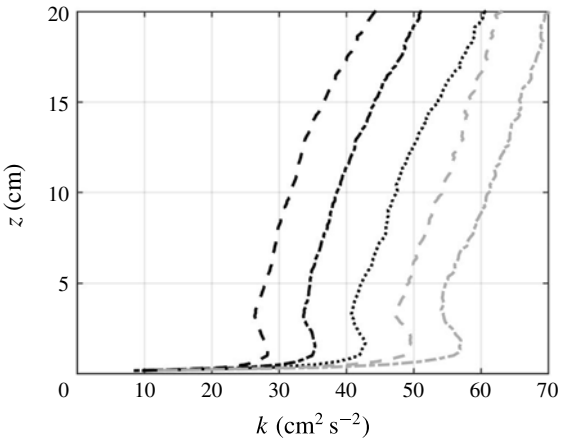

FIGURE 6. Turbulent kinetic energy profiles for $\Phi_{on} = 3.1\,\%$, $T_{on} = 0.8$ s (−−), 1.0 s (−·), 1.2 s (· · ·); 1.4 s (−− grey), 1.6 s (−· grey). 16 × 16 RAJSA.

As in the literature review of Variano *et al.* (2004), we consider M_1 and M_3, the ratios of mean velocity to r.m.s. velocity in the bed-parallel and bed-normal directions, respectively, to evaluate the strength of secondary flows. Clearly, if averaged spatially over the entire facility, both M_1 and M_3 tend to zero, as any flow must be balanced by a return flow in another location. Because of this, we consider temporally averaged values of M_1 and M_3 across the entire FOV before computing $M_1 = (\langle U\rangle/\langle u'\rangle)$ and $M_3 = (\langle W\rangle/\langle w'\rangle)$ to ensure that averaging along the x-axis accurately represents typical values across the entire width of the FOV. Additionally, we consider a relative mean flow strength M^*, defined as the ratio of the mean kinetic energy $(\langle U\rangle^2 + (1/2)\langle W\rangle^2)$ to the turbulent kinetic energy.

Across all cases with both the 8 × 8 RASJA and 16 × 16 RASJA, we find M^* consistently less than 3 % throughout the FOV. We find typical values of M_1 of approximately 4 %, and typical values of M_3 around 7 %. Values of M^* are on average 0.8 % for the 8 × 8 RASJA and 1 % with the 16 × 16 RASJA. M_1, M_3, and M^* are not correlated with T_{on}. Additional details are presented in Johnson (2016). As secondary flows were found to be negligible by Variano & Cowen (2008) for flows in which M_1 and M^* do not exceed 5 %, both RASJAs perform adequately to study turbulence with negligible recirculations or secondary flows.

3.3. *Integral length scale*

Using PIV data, we compute the integral length scale, $\mathcal{L}$, as the characteristic length scale of the largest eddies of our turbulent flow. At every height above the bed, we compute the spatial longitudinal autocorrelation function

$$a_{11,1}(r) = \frac{\left\langle u(x_c - \frac{r}{2})u(x_c + \frac{r}{2})\right\rangle}{\left(\left\langle u(x_c - \frac{r}{2})^2\right\rangle \left\langle u(x_c + \frac{r}{2})^2\right\rangle\right)^{1/2}} \tag{3.1}$$

such that r is the spatial separation along the horizontal axis, as presented in Variano & Cowen (2008). Similarly, the transverse autocorrelation $a_{33,1}(r)$ is computed as

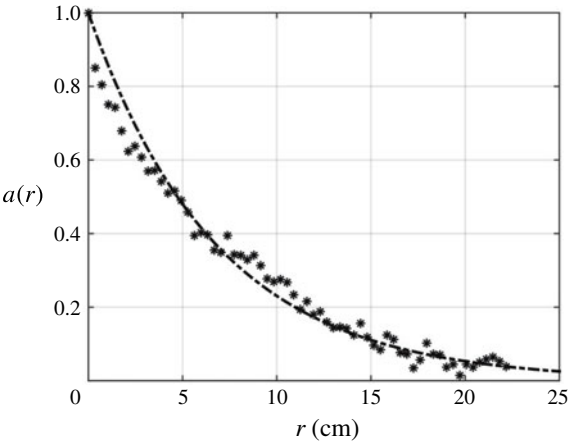

FIGURE 7. Exponential curve fit (−·) to autocorrelation function $a_{11,1}(*)$. $T_{on} = 4$ s, $\Phi_{on} = 6.25\,\%$, $z = 13.02$ cm, 8×8 RASJA.

a function of w. For sufficiently large measurement regions, $a(r)$ converges to zero with increasing r, and the integral length scale can be computed directly as $\mathcal{L}_L = \int a_{11,1}(r)\,\mathrm{d}r$ at every height in the FOV. However, our FOV is too narrow to consistently capture this convergence, so we fit an exponential curve $a_L(r) = e^{-r/\mathcal{L}_L}$ to the longitudinal autocorrelation data, as shown in figure 7, to determine the fit parameter $\mathcal{L}_L$ in $a_L(r)$ that best matches $a_{11,1}(r)$. This modelled curve fit consistently shows coefficient of determination R^2 values of 0.99 between $a_L(r)$ and $a_{11,1}(r)$, demonstrating an excellent match to the autocorrelation data.

By assuming isotropy to address the transverse autocorrelation, we invoke the relationship from Pope (2000),

$$a_{33,1}(r) = a_{11,1}(r) + \frac{1}{2} r \frac{\partial}{\partial r} a_{11,1}(r), \tag{3.2}$$

which is modelled as $a_T(r) = e^{-r/\mathcal{L}_t}(1 - r/2\mathcal{L}_t)$ according to the exponential fit for $a_L(r)$. Using this model, we solve for $\mathcal{L}_t$, as $\mathcal{L}_T = (1/2)\mathcal{L}_t$ from assuming isotropy (Pope 2000). Although this is an appropriate assumption in the mixed region of the flow (to be discussed further in § 4), this assumption is violated near the bed, in particular below the point where $u' > w'$ due to the kinematic boundary condition. The modelled curve fit has R^2 values of 0.99. Sample profiles of the longitudinal and transverse integral length scales are shown in figure 8.

Although the integral length scale in experimental turbulence facilities is often thought to scale strictly with the grid spacing or other geometric constraints, as discussed in Hopfinger & Toly (1976), it has been shown that the integral length scale can be controlled by varying the parameters of an active grid in wind tunnel experiments (Makita 1991; Mydlarski & Warhaft 1996). Additionally, the integral length scale is strongly dependent upon distance from the grid in both GST (Thompson & Turner 1975) and moving-bed experiments (Thomas & Hancock 1977).

We consider the integral length scale of the turbulent flow to be equivalent to the longitudinal integral length scale in the mixed region of the tank (to be discussed in the following section) where the energetics and structure of the turbulence are independent of z. We find that we are able to control $\mathcal{L}$ by varying T_{on}, as observed

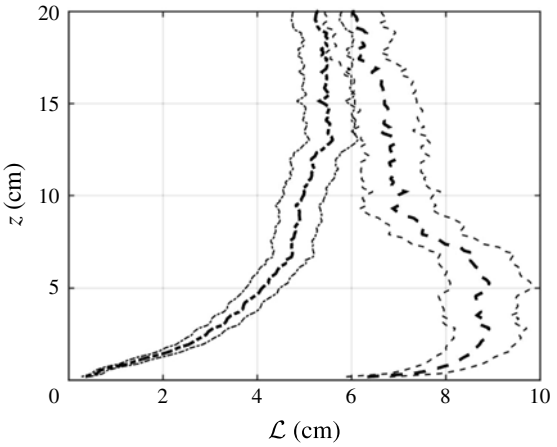

FIGURE 8. Profiles of $\mathcal{L}_L(--)$ and $\mathcal{L}_T(-\cdot)$ with 95 % confidence intervals for $T_{on} =$ 4 s, $\Phi_{on} = 6.25\,\%$, 8×8 RASJA.

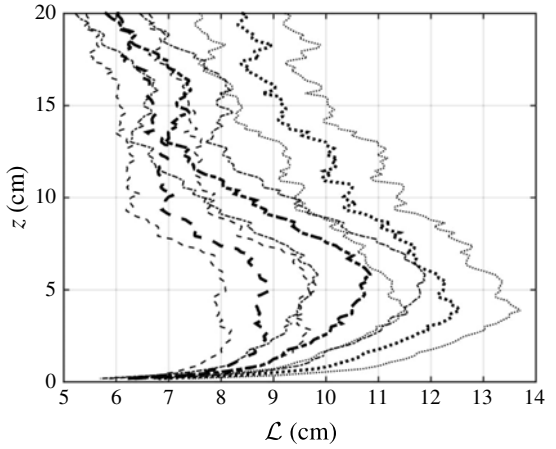

FIGURE 9. Profiles of $\mathcal{L}_L$ with 95 % confidence intervals for $T_{on} = 4$ s $(--)$, 6 s $(-\cdot)$, 8 s $(\cdots)$, $\Phi_{on} = 6.25\,\%$, 8×8 RASJA.

in figure 9. Longer T_{on} means the jets penetrate deeper into the flow, injecting more energy, enhancing the degree of turbulent stirring and increasing the integral length scale. Therefore changing T_{on} is equivalent to changing the geometry within a facility, and is a suitable manner in which to vary $\mathcal{L}$ using a single RASJA.

For comparison to other experimental and theoretical data, we also compute the integral length scale via the scaling determined relationship $\mathcal{L}^* = k^{3/2}/\epsilon$, where ϵ is the dissipation rate of turbulent kinetic energy, to be discussed in depth in § 5. As this is not a direct measurement of the integral length scale, it results in values that are within the right order-of-magnitude only of the exponential fit method. Results are presented in § 4.

Because the variations in T_{on} in the 16×16 RASJA are very small compared to those in the 8×8 RASJA, incremented by 0.2 s rather than 2 s, we do not observe discernible differences in the resulting integral length scale measured by the

exponential fit to the autocorrelation function. Although $\mathcal{L}_L$ does not strictly increase with T_{on}, a trend of increasing $\mathcal{L}^*$ is observed with T_{on}, and the incremental changes suggest that changing T_{on} should still result in changing integral length scale as long as the interval in T_{on} is sufficiently large. Due to the different geometry and energetics of the flow between the two facilities, however, we do observe noticeably smaller $\mathcal{L}$ in the 16×16 RASJA as compared to the 8×8 RASJA. Resulting values of $\mathcal{L}$, $\mathcal{L}_T$, and $\mathcal{L}^*$ will be presented in the following section.

3.4. *Integral time scale*

As in Peters (1999), we estimate the integral time scale as

$$\tau_{int} = \frac{\mathcal{L}}{\sqrt{k}} \tag{3.3}$$

or the ratio of the integral length scale to the r.m.s. turbulent velocity scale. For the 15 cases considered with the 8×8 RASJA, we find an average τ_{int} of 1.17 s, which is close to our PIV sampling frequency, F_s of 1 Hz that was selected to achieve uncorrelated samples. There is no distinct trend between the sunbathing parameters and τ_{int}. With the 16×16 RASJA, τ_{int} is reduced to 0.67 s.

4. Structure of turbulence within the facility

Given the resulting profiles of r.m.s. velocities, turbulent kinetic energy and integral length scales, we can better understand the structure of the turbulence in the facility as it develops with distance from the jets and proximity to the bed with each of the jet arrays. As shown in the caricature presented in figure 1, the tank is composed of several distinct regions. From top to bottom, the flow is made up of a jet forcing region, in which the instantaneous on–off states surrounding the jet orifice plane drive local recirculations, a jet merging region, in which the jet wakes and return flows continue to generate strong upward and downward flows while interacting with one another, a mixed region, where the flow no longer feels the on–off state of each jet, but instead is already stirred into horizontally homogeneous nearly isotropic turbulence, and below, a bed-influenced region, where the flow is strongly altered due to its interaction with the bed. The bed-influenced region, or boundary layer, consists of a ‘source region’, in which turbulent fluctuations respond to the presence of the bed due to the kinematic effect, a buffer region in which turbulence levels decay from peak energy levels towards zero, and a viscous sublayer immediately above the solid bed.

We find that when using the two different RASJAs, we observe all of these regions, although there are additional details within and between these regions that we will present, based on each RASJA. We compare our results with theoretical formulations for shear free turbulence at a solid boundary (Hopfinger & Toly 1976; Hunt & Graham 1978; Hunt 1984), and experimental results from a GST with a free surface (Brumley & Jirka 1987) to elucidate the different flow features of each facility. In addition to evaluating the development of turbulence with distance from the jets and proximity to the bed, we also re-examine the resulting profiles of r.m.s. velocity and integral length scale, in particular, to comment on the isotropy of the flow.

Φ_{on} (%)	T_{on} (s)	u' $\left(\frac{\text{cm}}{\text{s}}\right)$	95 % CI	w' $\left(\frac{\text{cm}}{\text{s}}\right)$	95 % CI	k $\left(\frac{\text{cm}^2}{\text{s}^2}\right)$	95 % CI
6.25	4	4.08	[4.06, 4.09]	5.53	[5.51, 5.55]	31.95	[31.79, 32.12]
6.25	6	4.54	[4.52, 4.56]	6.32	[6.29, 6.34]	40.57	[40.37, 40.77]
6.25	8	5.19	[5.17, 5.21]	7.01	[6.98, 7.03]	51.47	[51.22, 51.73]

TABLE 1. Turbulent (r.m.s.) velocities and turbulent kinetic energy. All values shown are the mean value of the statistic in the mixed region from PIV data. 8×8 RASJA.

Φ_{on} (%)	T_{on} (s)	$\mathcal{L}_L$ (cm)	95 % CI	$\mathcal{L}_T$ (cm)	95 % CI	$\mathcal{L}^* = \frac{k^{3/2}}{\epsilon}$ (cm)
6.25	4	6.80	[6.17, 7.50]	5.32	[4.86, 5.86]	21.66
6.25	6	7.44	[6.75, 8.22]	6.48	[5.96, 7.07]	26.10
6.25	8	9.71	[8.85, 10.64]	6.10	[5.60, 6.69]	30.30

TABLE 2. Integral length scale results. All values shown are the mean value of the statistic in the mixed region from PIV data. 8×8 RASJA.

4.1. *Mixed region*

4.1.1. *The* 8×8 *RASJA*

Profiles of u', w' and k show a fairly straightforward structure of the turbulence facility with the 8×8 RASJA. In figures 3 and 5, we observe u' and k to be constant with z for much of the upper one half to two thirds of the FOV. If we also consider profiles of the integral length scale, we observe $\mathcal{L}_L$ also approximately constant for $z > 1.5\mathcal{L}_L$. This is the lower bound of our mixed region. As z increases above this height, u' continues to be relatively independent of z, and so it appears that in experiments with the 8×8 RASJA, the mixed region extends to the top of the FOV. We define metrics with subscript m as the mean of those values in the mixed region; for example, u'_m is the mean of the horizontal r.m.s. velocity in the mixed region. A sample of resulting statistics is summarized in tables 1 and 2.

In the mixed region, we expect the flow to be nearly isotropic, as it is fully mixed and unaffected by the boundary below. The ratio w'/u' provides a measure of isotropy. Though we do not achieve unity, we find a ratio $w'/u' = 1.29$; this is consistent with isotropy ratios observed in other facilities with forcing from only one side of the tank. Variano & Cowen (2008) found an isotropy ratio of 1.27, and several GST experiments found ratios of 1.1–1.3 (Hopfinger & Toly 1976) and 1.4 (McDougall 1979). Due to the forcing along the vertical axis in particular, one would expect to observe $w'/u' > 1$ away from boundaries.

We can also look to the profiles of integral length scale to evaluate the assumption of isotropy used in measuring the transverse integral length scale. Our assumption of isotropy at both small and energy-containing scales ought to lead us to the relationship $\mathcal{L}_L/\mathcal{L}_T = 2$ (Pope 2000). However, the data produce a relationship of approximately $\mathcal{L}_L/\mathcal{L}_T = 1.29$ in the mixed region across the 15 cases considered with the 8×8 RASJA, which is consistent with the ratio of 1.19 reported in Variano & Cowen (2008).

4.1.2. *The* 16×16 *RASJA*

When using the 16×16 RASJA, the flow regions are organized slightly differently. Recall that the 16×16 RASJA is non-dimensionally 'deeper', with $H/J = 13$,

Φ_{on} (%)	T_{on} (s)	u' $\left(\frac{\text{cm}}{\text{s}}\right)$	95 % CI	w' $\left(\frac{\text{cm}}{\text{s}}\right)$	95 % CI	k $\left(\frac{\text{cm}^2}{\text{s}^2}\right)$	95 % CI
3.1	0.8	4.61	[4.59, 4.63]	5.68	[5.66, 5.70]	37.49	[37.30, 37.69]
3.1	1.0	5.03	[5.01, 5.05]	6.25	[6.23, 6.27]	44.89	[44.65, 45.13]
3.1	1.2	5.51	[5.49, 5.53]	6.86	[6.84, 6.89]	53.99	[53.69, 54.29]
3.1	1.4	5.64	[5.62, 5.67]	7.33	[7.30, 7.35]	58.74	[58.41, 59.06]
3.1	1.6	5.97	[5.95, 6.00]	7.78	[7.75, 7.81]	65.98	[65.61, 66.34]

TABLE 3. Turbulent (r.m.s.) velocities and turbulent kinetic energy. All values shown are the mean value of the statistic in the mixed region from PIV data. 16×16 RASJA.

Φ_{on} (%)	T_{on} (s)	$\mathcal{L}_L$ (cm)	95 % CI	$\mathcal{L}_T$ (cm)	95 % CI	$\mathcal{L}^* = \frac{k^{3/2}}{\epsilon}$ (cm)
3.1	0.8	4.63	[4.29, 5.27]	3.59	[3.44, 4.16]	10.45
3.1	1.0	5.19	[4.71, 5.84]	3.83	[3.69. 4.49]	11.64
3.1	1.2	4.65	[4.29, 5.26]	3.57	[3.37, 4.20]	11.61
3.1	1.4	4.52	[4.21, 5.22]	4.41	[4.39, 5.37]	12.83
3.1	1.6	4.75	[4.37, 5.42]	4.53	[4.41, 5.38]	13.35

TABLE 4. Integral length scale results. 16×16 RASJA.

compared to $H/J = 7.1$ with the 8×8 RASJA. With the 16×16 RASJA, the lower bound of the mixed region is again observed at $z = 1.5\mathcal{L}_L$, where u' and $\mathcal{L}_L$ are relatively independent of z. Interestingly, although u' is constant in this range, k decreases with distance from the jets. We will explore this further in the coming section. Above the mixed region, there is a decay in u', w' and k with decreasing z (or increased distance from the jets). This is noticeably different between the two RASJAs, as shown when comparing figures 5 and 6. As mixing occurs a distance of $6J$ from the jet orifice plane, we are confident that jets are fully merged prior to reaching the top of the FOV, and that likely the significantly greater H/J parameter generates this different energetic structure.

Resulting values of r.m.s. velocities, turbulent kinetic energy, and integral length scale computed in the mixed region are presented in tables 3 and 4. We observe similar behaviour regarding isotropy ratios, with $w'/u' = 1.26$ and $\mathcal{L}_L/\mathcal{L}_T = 1.20$ across all 5 cases with the 16×16 RASJA.

We are interested in exploring the rate of decay observed with the 16×16 RASJA and in characterizing the turbulence in the mixed region directly above the boundary layer. Recalling the decay relationship proposed by Hopfinger & Toly (1976) suggesting that turbulence facilities with turbulence generated by oscillating grids should show decay of u' and w' away from the source, we draw comparisons between the results obtained in our two facilities to determine the relevance of the concept of decay away from the RASJAs.

As shown in figures 10 and 11, turbulent decay is not always an accurate representation of the observations in a facility with an oscillating grid or random jet array, and we are excited to be able to generate such different flow patterns with similarly designed facilities. For experiments with the 8×8 RASJA, with $H/J = 7.1$, both u' and w' are nearly independent of z as discussed previously, aligning well with curves from Hunt & Graham (1978). However, with the 16×16 RASJA, with $H/J = 13$, there is a much clearer region of decay for both u' and w' that closely aligns with the Hopfinger & Toly (1976) relationship for $z/H > 0.15$. Although

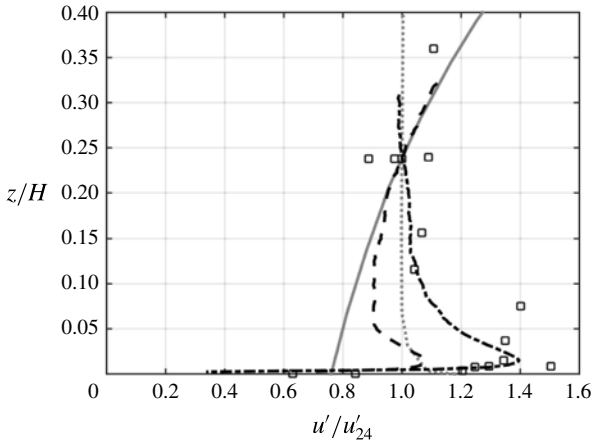

FIGURE 10. Comparison of experimental u' data. $T_{on} = 4$ s, $\Phi_{on} = 6.25\,\%$, 8×8 RASJA ($-\cdot$), $T_{on} = 0.8$ s, $\Phi_{on} = 3.1\,\%$, 16×16 RASJA ($--$) with Brumley & Jirka (1987) GST data (□), Hopfinger & Toly (1976, $-$ grey), and Hunt & Graham (1978) ($\cdots$ grey). Vertical axis normalized by jet height $H = 71$ cm and $H = 65$ cm for 8×8 and 16×16 RASJAs, respectively; horizontal axis normalized to average 1 at $z/H = 24\,\%$, as in Brumley & Jirka (1987).

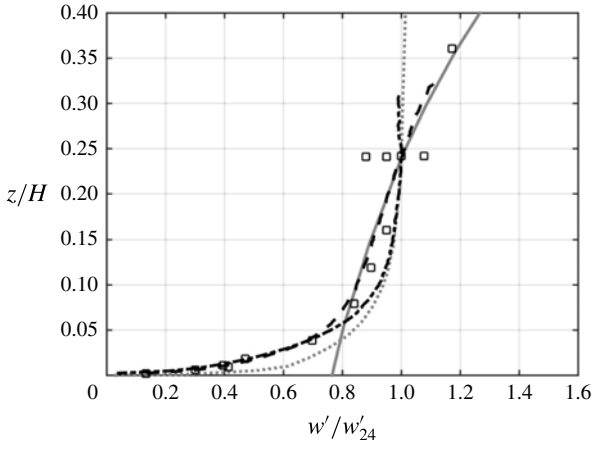

FIGURE 11. Comparison of experimental w' data. See previous figure for legend.

figures 10 and 11 only show one profile from each RASJA, all curves collapse well within their respective facility. However, we do not see collapse between the facilities, in part because of the type of non-dimensionalization performed in this figure. As in the convention of Brumley & Jirka (1987), the profiles are normalized according to the value of u' at which $z/H = 0.24$, which is not in the mixed region with the 16×16 RASJA. We also note that because the two RASJA experiments shown have similar values of k, u' and w' near the bed, the flow structure of the facility appears more closely linked to the proximity of the turbulence source to the bed, or rather, the ratio H/J, than to the turbulence levels themselves.

4.2. *Bed-influenced region*

Beneath the mixed region, there is a clear intercomponent energy transfer as bed-normal velocity fluctuations begin to decay and bed-parallel velocity fluctuations

rise as a result of interactions with the solid boundary, describing a kinematic effect. We term the flow between the mixed layer and bed the boundary layer, as the flow patterns we observe are a direct result of the flow encountering a solid interface.

Considering profiles of u' and w' with the 8×8 RASJA, there is a gradual increase in u' beneath the mixed layer, or beneath approximately $z = 1.5\mathcal{L}$. This continues until approximately $z/\mathcal{L} = 0.5$, at which point $u' = w'$. This region is the transition between the mixed region and the source region. Interestingly, we do not observe this transition when using the 16×16 RASJA, but instead observe a sharper transition where u' is constant then rapidly increases beneath the point at which $u' = w'$.

Beneath the crossing point at which point $u' = w'$, we observe a significant decrease in bed-normal velocity fluctuations as bed-parallel fluctuations rise due to the kinematic boundary condition and inability of bed-normal motions to penetrate the bed. The anisotropy between u' and w' increases until roughly $z/\mathcal{L} = 0.15$, at which point we observe a peak in both u' and k. The region for which $0.15 < z/\mathcal{L} < 0.5$ is the source region, where the presence of the bed induces significant intercomponent energy transfer and dynamic turbulent splats (Perot & Moin 1995*a*). We also recall that whereas $\mathcal{L}_T$ decreases towards the bed in the boundary layer, there is a notable increase in $\mathcal{L}_L$ due to the significant restructuring of energy from homogeneous isotropic motions to strongly energetic bed-parallel motions throughout the boundary layer.

Below $z/\mathcal{L} = 0.15$, w' continues to diminish to zero, while u', k, and dissipation, which we will consider in the following section, rapidly decay to zero due to the no-slip boundary condition. In physical space, this region encompasses a thickness of the order of 1 cm, and so clearly this is not a true viscous sublayer. We term the region beneath $z/\mathcal{L} = 0.15$ as the buffer region, and it extends as high as the greatest bed-parallel energy that arises from the kinematic boundary condition. This region is comparable to the viscous region described in Hunt & Graham (1978), though in our experiments it extends beyond a true viscous region. As we will show in the following section, the bottom-most layer within this region is our viscous sublayer, in which we see the final decay to zero for the first-order flow statistics considered.

Looking again at figures 10 and 11, we can compare prior theory and experimental data in the boundary layer. We find the expected decay in GST theory neglects the enhancement of u' in the kinematic region and the viscous decay of u' and w' at the bed that we observe with the RASJAs. Instead, our data from both experiments are better aligned with the experimental GST results of Brumley & Jirka (1987) and theory of Hunt & Graham (1978) in the measurement region considered, even though the Brumley & Jirka (1987) experiments consider the mean shear free turbulent boundary layer at a free surface rather than a flat plate. A free surface differs from a flat plate boundary in that there is free slip and a deformable free surface, leading to potentially weaker intercomponent energy transfer near the surface and minimal viscous decay at the surface itself. Even with these differences, the Brumley & Jirka (1987) experiments show a significant transfer from surface-normal to surface-parallel energy, with u'/u'_{24} values around 1.4, compared to 0.8 predicted by the combined Hopfinger & Toly (1976) and Hunt & Graham (1978) theories.

It has been suggested that turbulence at a free surface can generate conditions in which $\partial w'/\partial z = 0$ at a surfactant-contaminated surface (Shen, Yue & Triantafyllou 2004; Khakpour, Shen & Yue 2011), and that such a contaminated surface may model a solid boundary due to reduced slip at the boundary (Herlina & Wissink 2016). However, we do not observe this behaviour in our experimental turbulence facility. At the resolution of our PIV experiments (0.176 cm), it appears that both u' and w'

approach zero at non-zero vertical gradients. Indeed, it is likely extremely difficult to fully prevent surfactants from contaminating a free surface, even in a controlled laboratory environment (Variano & Cowen 2008), which perhaps contributes to the significant increase in u' in the Brumley & Jirka (1987) experiments that agree so well with our results with the 8×8 RASJA in the boundary layer, despite the mobility of the free surface that differs critically from a solid boundary that necessitates significant intercomponent energy transfer.

5. Turbulent kinetic energy balance

In order to understand the dynamics and energy balance of the unique boundary layer that forms in the absence of a mean flow or mean boundary-induced shear, we look to the turbulent kinetic energy budget,

$$\frac{\partial k}{\partial t} + \langle U_j \rangle \frac{\partial k}{\partial x_j} = -\frac{1}{\rho_0}\frac{\partial \langle u_i p \rangle}{\partial x_i} - \frac{1}{2}\frac{\partial \langle u_j u_j u_i \rangle}{\partial x_i} + \nu \frac{\partial^2 k}{\partial x_j^2} - \langle u_i u_j \rangle \frac{\partial \langle U_i \rangle}{\partial x_j} - \nu \left\langle \frac{\partial u_i \partial u_i}{\partial x_j \partial x_j} \right\rangle, \quad (5.1)$$

which explores the relationship between unsteady turbulent kinetic energy, advection, pressure diffusion, turbulent transport, molecular viscous transport, production and dissipation.

In channel flow, one would expect to see a balance between the dissipation rate and production of k, known as local equilibrium, in the boundary layer (Spalart 1988). Dissipation and production are typically of opposite sign and of greatest magnitude, relative to the other terms in the budget. Turbulent transport and viscous diffusion follow in magnitude, with the latter of particular significance at the wall, where it balances dissipation. Pressure diffusion is typically an order-of-magnitude smaller than dissipation and production. Pressure, production, and turbulent transport are equal to zero at the wall in a shear-driven flow.

However, in the absence of a mean flow, we observe a drastically different balance. Viscous transport and advection are approximately two orders-of-magnitude less than the dissipation, production, and turbulent transport terms, as shown in Johnson (2016), and they are thus neglected in this analysis. With continuous turbulent forcing from above, k is stationary in time and its temporal derivative is also neglected.

Perfect isotropy does not exist in our flow, nor in many other flows where it is assumed to exist for the purpose of deriving higher-order metrics, so we compute dissipation, production, and turbulent transport directly from PIV data. This avoids the need for assuming isotropy as is required in several other common methods, such as the second-order structure function or spatial spectra compensation. In the absence of direct measurements of pressure, we determine pressure diffusion as the residual of the remaining terms in the budget in order to understand, at minimum, the order-of-magnitude that pressure plays in the boundary layer. Furthermore, we use our dissipation results from PIV analysis to explore the use of Eulerian frequency spectra to compute dissipation from point measurements when access to spatial data is limited.

5.1. *Dissipation*

5.1.1. *Direct method*

To accurately compute dissipation, following Cowen & Monismith (1997), we use the direct formulation $\epsilon \equiv 2\nu\langle S_{ij}S_{ij}\rangle$, with $S_{ij} \equiv (1/2)(\partial u_i/\partial x_j) + (\partial u_j/\partial x_i)$. This method

is advantageous in that there are no empirical constants or isotropy requirements. In the boundary layer under investigation, we know the flow is anisotropic near the bed, as is evident when considering the intercomponent transfer from w' to u' presented in figures 3 and 4. Although the flow is more isotropic in the mixed region, we still observe weak anisotropy, due to the vertical forcing of the facility. Thus, we cannot assume that horizontal and vertical statistics are equivalent, which is a key requirement in the alternate methods of computing ϵ, explored further in Johnson (2016).

Because we can only directly measure $\partial u/\partial x$, $\partial u/\partial z$, $\partial w/\partial x$, and $\partial w/\partial z$ from PIV data, we invoke continuity, as in Doron *et al.* (2000), such that

$$\overline{\left(\frac{\partial v}{\partial y}\right)^2} = \overline{\left(-\frac{\partial u}{\partial x} - \frac{\partial w}{\partial z}\right)^2} = \overline{\left(\frac{\partial u}{\partial x}\right)^2} + \overline{\left(\frac{\partial w}{\partial z}\right)^2} + 2\overline{\left(\frac{\partial u}{\partial x}\frac{\partial w}{\partial z}\right)}. \tag{5.2}$$

Radial symmetry allows for substitutions $\partial v/\partial x = \partial u/\partial x$, $\partial u/\partial y = \partial u/\partial x$, $\partial v/\partial z = \partial u/\partial z$, and $\partial w/\partial y = \partial w/\partial x$, which produces a two-dimensional radially symmetric direct formulation

$$\epsilon = 2\nu\left[4\overline{\left(\frac{\partial u}{\partial x}\right)^2} + \overline{\left(\frac{\partial u}{\partial z}\right)^2} + \overline{\left(\frac{\partial w}{\partial x}\right)^2} + 2\overline{\left(\frac{\partial w}{\partial z}\right)^2} + 2\overline{\left(\frac{\partial u}{\partial x}\frac{\partial w}{\partial z}\right)} + 2\overline{\left(\frac{\partial u}{\partial z}\frac{\partial w}{\partial x}\right)}\right]. \tag{5.3}$$

The cross-terms, $\overline{((\partial u/\partial x)(\partial w/\partial z))}$ and $\overline{((\partial u/\partial z)(\partial w/\partial x))}$, only account for approximately 3 % of the total dissipation in the direct method, and diagonal elements of S_{ij} dominate. This relationship holds in both the isotropic mixed region and anisotropic boundary layer.

Spatial resolution is of critical importance in using the direct method, as noise is amplified if the resolution is refined beyond the smallest length scales, and PIV interrogation regions that are too large average the turbulent length scales causing an underestimation of the dissipation rate. Given our spatial resolution of 9η, where η represents the Kolmogorov length scale (to be explored further in § 5.5), an integration of the universal spectrum proposed by Pao (1965) suggests that computing the spatial derivatives directly from our PIV data is sufficient for capturing 92 % of the total dissipation with the direct method (Cowen & Monismith 1997). Thus, resulting values are scaled up by a factor of 1.09 to account for this slight under-resolution.

Typical resulting profiles of dissipation computed directly are shown in figure 12, revealing that dissipation is essentially constant as a function of height except very near the bed in the buffer region, beneath approximately $z/\mathcal{L} = 0.15$, where the magnitude of dissipation increases dramatically due to the no-slip boundary condition. In figure 12, we see reasonable collapse of three selected ϵ profiles, when normalized by their values in the mixed region. Hunt (1984) predicts $\epsilon \propto z^{-1}$ as $z/\mathcal{L}$ approaches zero, and indeed it appears our data fall between exponential values of $-3/4$ and -1 across all experimental cases.

As a means of validating our calculation of ϵ, we consider the energy spectrum as computed from bed-parallel PIV data. Specifically, we compute the dissipation spectrum, as in Pao (1965), Cowen & Monismith (1997) and Pope (2000), among others. A sample dissipation spectrum computed in the mixed region is shown in figure 13. The dissipation spectrum is normalized by u_η^3, where the Kolmogorov velocity scale $u_\eta = (\nu\epsilon)^{1/4}$ is computed in the mixed region. We observe strong agreement between the modelled dissipation spectrum and the present experimental data, noting high wavenumber noise for $\kappa\eta > 0.3$.

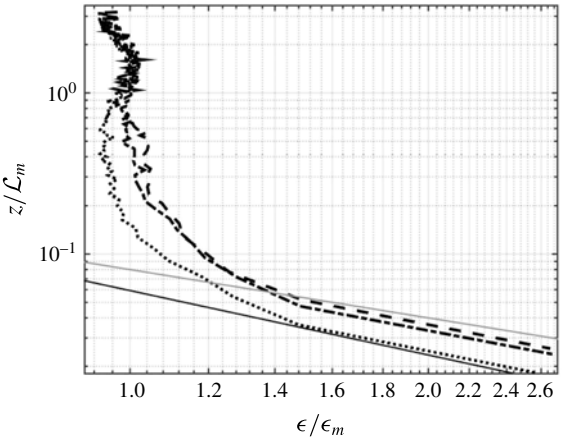

FIGURE 12. Normalized dissipation profiles with $\epsilon \propto z^{-3/4}$ (−), $\epsilon \propto z^{-1}$ (− grey). $T_{on} = 4$ s (−−), 6 s (−·), 8 s (···), $\Phi_{on} = 6.25\,\%$, 8×8 RASJA.

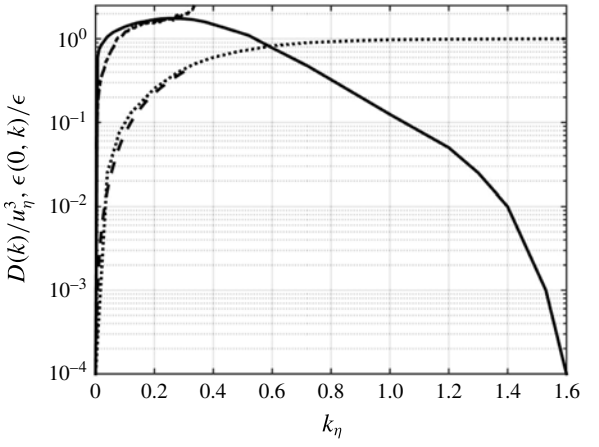

FIGURE 13. Normalized dissipation spectrum (− as in Pope (2000); −· present data) and cumulative dissipation (··· as in Pope (2000); −− present data) normalized by ϵ_m as computed by the direct method. Present experimental data shown for $z = 11.8$ cm, $\Phi_{on} = 6.25\,\%$, $T_{on} = 4$ s, 8×8 RASJA.

By integrating the dissipation spectrum, we can also compute the cumulative dissipation, as shown in figure 13. Although the spectrum from the data does not extend as far as $\kappa\eta \approx 1.6$, where approximately 100 % of the dissipation is captured, we see agreement of 93 % between our data and the modelled curve for $\kappa\eta < 0.3$ when normalizing the cumulative dissipation by the value of ϵ_m computed via the direct method.

5.1.2. *Eulerian frequency spectra*

Whereas several methods are available from which to compute dissipation rates from spatial PIV data, it is valuable to further develop methods of determining dissipation from point measurements such as ADV. Such instruments are typically

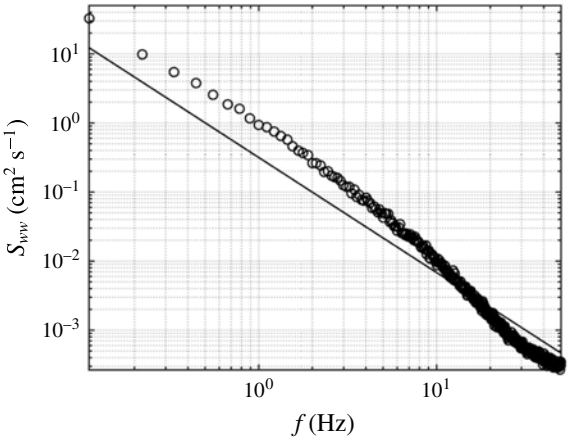

FIGURE 14. Frequency spectrum of vertical velocity from 100 Hz ADV measurement at $z = 12$ cm, 200 ensemble averages. $T_{on} = 4$ s, $\Phi_{on} = 6.25\,\%$, 8×8 RASJA.

more readily deployable in field experiments or in laboratory set-ups with limited visual access. Without a mean flow, we are unable to convert temporal records to spatial records via Taylor's frozen turbulence hypothesis, and so we instead turn to Eulerian frequency spectra (Tennekes 1975).

Temporal frequency spectra, an example of which is shown in figure 14, are computed from 100 Hz ADV records taken in the mixed region at a point $z = 12$ cm above the bed for experiments using the 8×8 RASJA only. Although the spectra are only plotted up to the Nyquist frequency, all frequency spectra shown are normalized such that the integral of the spectra over $\omega \in (-\infty, \infty)$ is equal to the variance of the velocity signal. The S_{ww} spectra are least affected by noise in the configuration used, due to the geometric considerations of the ADV, so we are only considering the bed-normal velocity spectra in our analysis.

Through a simple scaling of 2π, temporal frequency spectra are transformed into Eulerian frequency spectra; a sample compensated Eulerian frequency spectrum is shown in figure 15. By identifying the plateau of the compensated spectrum, we utilize the relationships introduced by Tennekes (1975)

$$E(\omega) = B_o \epsilon^{2/3} (\sqrt{2k})^{2/3} \omega^{-5/3} \tag{5.4}$$

and further developed by Kit, Fernando & Brown (1995) as

$$E(\omega) = B_1 \epsilon^{2/3} w'^{2/3} \omega^{-5/3} \tag{5.5}$$

to deduce the empirical constants B_0 and B_1 that relate dissipation to the Eulerian frequency spectra.

Few experimental studies have been conducted to determine the empirical fit coefficients. In GST studies, De Silva & Fernando (1994) found a value of $B_1 = 8$. In these experiments r.m.s. velocities were estimated by the Hopfinger & Toly (1976) equations and scaling arguments rather than measured directly in the facility. Later GST experiments by Kit *et al.* (1995) used a two-component fibre optic laser Doppler velocimeter and reported a value of coefficient $B_1 = 0.7$ for vertical velocity records after using isotropic strain rate relationships to determine the dissipation rate

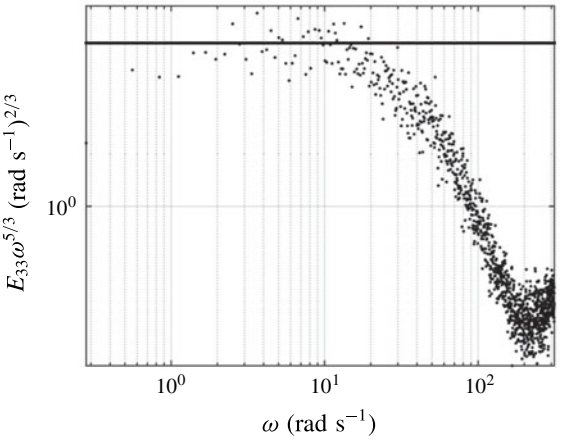

FIGURE 15. Eulerian frequency spectrum of vertical velocity from 100 Hz ADV measurement at $z = 12$ cm, 80 ensemble averages. $T_{on} = 4$ s, $\Phi_{on} = 6.25\,\%$, 8×8 RASJA.

Φ_{on} (%)	T_{on} (s)	ϵ $\left(\frac{\text{cm}^2}{\text{s}^3}\right)$	B_o	B_1
6.25	4	8.34	0.12	0.17
6.25	6	9.90	0.13	0.18
6.25	8	12.19	0.16	0.23

TABLE 5. Resulting values of dissipation, calculated directly, and coefficients for Eulerian frequency spectra estimates of dissipation. Values of dissipation are averaged in the mixed region. 8×8 RASJA.

from the vertical velocity records. Variano & Cowen (2008) reported $B_0 = 0.23$ and $B_1 = 0.35$ for a vertical velocity time series, with dissipation rates computed from the second-order longitudinal structure function and r.m.s. velocities computed from PIV measurements and turbulent spectra computed from ADV data.

To compute current estimates of B_0 and B_1, our dissipation estimate comes from the corrected direct method using PIV data, whereas $E(\omega)$, w' and k come directly from ADV measurements. When averaged across all 15 trials, we find resulting values of $B_0 = 0.14$ with a 95 % confidence interval of [0.13, 0.14] and $B_1 = 0.19$ with a 95 % confidence interval of [0.18, 0.20]. These values satisfy the Tennekes (1975) and Kit *et al.* (1995) models, respectively, for vertical velocity measurements.

5.2. *Turbulent transport*

Because the spatial resolution of the analysed PIV data is sufficient to directly compute spatial derivatives for higher-order statistical analysis such as dissipation, we can also directly compute the remaining terms in the turbulent kinetic energy balance such as turbulent transport, $T = -(1/2)(\partial \langle u_j u_j u_i \rangle / \partial x_i)$. We invoke radial symmetry to simplify our equation to

$$T = -\frac{1}{2}\left[4\frac{\partial \langle uuu \rangle}{\partial x} + 2\frac{\partial \langle wwu \rangle}{\partial x} + 2\frac{\partial \langle uuw \rangle}{\partial z} + \frac{\partial \langle www \rangle}{\partial z}\right]. \tag{5.6}$$

Φ_{on} (%)	T_{on} (s)	ϵ $\left(\frac{\text{cm}^2}{\text{s}^3}\right)$
3.1	0.8	20.17
3.1	1.0	23.90
3.1	1.2	31.08
3.1	1.4	31.33
3.1	1.6	35.93

TABLE 6. Resulting values of dissipation, calculated directly, averaged in the mixed region. 16×16 RASJA.

In doing so, we find negligible contributions from the $\partial/\partial x$ terms, as is expected from horizontal homogeneity. The triple correlation is an inherently noisy calculation, with relatively wide fluctuations throughout the FOV. The $\partial/\partial z$ terms fluctuate greatly, ranging across magnitudes of $-\epsilon$ to 2ϵ, and so a local median smoothing filter is applied to produce the final profile of T shown in figure 16. This is done via MATLAB's `medfilt1` function, a one-dimensional median filter, along 6 point-long segments.

5.3. *Production*

Similarly, we compute production, $P = -\langle u_i u_j \rangle \partial \langle U_i \rangle / \partial x_j$, which expands to

$$P = -\left[4\langle uu \rangle \frac{\partial \langle U \rangle}{\partial x} + 2\langle uw \rangle \frac{\partial \langle U \rangle}{\partial z} + 2\langle uw \rangle \frac{\partial \langle W \rangle}{\partial x} + \langle ww \rangle \frac{\partial \langle W \rangle}{\partial z}\right], \tag{5.7}$$

when invoking radial symmetry. Whereas $\langle uu \rangle$ and $\langle ww \rangle$ have significant magnitudes, as expected from our analysis of r.m.s. velocities previously, $\langle uw \rangle$ is essentially zero, with flow being equally likely to move in any radial direction. In considering the mean velocity gradients, we observe negligible contributions from $\partial \langle U \rangle / \partial x$ and $\partial \langle W \rangle / \partial x$ due to horizontal homogeneity. There are, however, weak contributions from the vertical gradients of both horizontal and vertical mean velocities due to the kinematic effect of the bed.

When combining the products of the mean velocity gradients and $\langle u_i u_j \rangle$ terms, the summation ultimately results in low levels of production. For all trials with the 8×8 RASJA, P is approximately zero at the bed. For the trials explored with $M^* < 1\,\%$, production remains negligible near the bed and in the mixed region, though not all 15 trials show such negligibly small values of P throughout the entire boundary layer. While more than half of these trials show near-zero magnitudes of production, some trials exhibit weak production in the source layer ranging from 2 to 6 $\text{cm}^2\,\text{s}^{-3}$. It appears that non-zero production results from non-zero $\partial \langle U \rangle / \partial x$ in particular, and additional details are explored in Johnson (2016). Even in cases with non-negligible values of P, the values of production obtained remain small relative to dissipation. Whereas production and dissipation are typically in balance in the near-wall region in boundary layers resulting from mean flows, the magnitude of production is at most only half as great as the magnitude of dissipation and is typically negligible in boundary layers absent mean flows. Because the computations of P are quite noisy about $P = 0$, a local median smoothing filter along 4 point segments is applied to the final profile shown in figure 16.

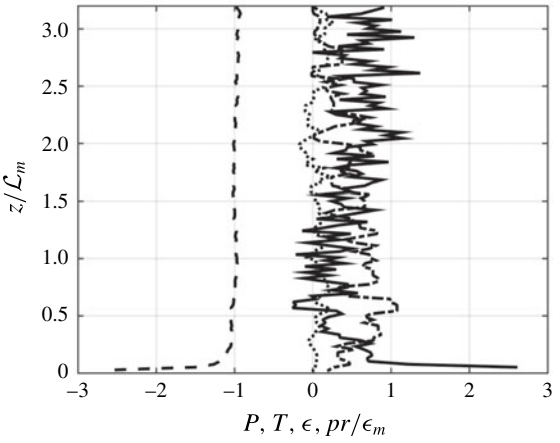

FIGURE 16. Dissipation (−−), turbulent transport (−·), production (· · ·), estimated pressure diffusion (−), non-dimensionalized by ϵ_m from direct method. T_{on} = 4 s, Φ_{on} = 6.25 %, 8 × 8 RASJA.

5.4. *Pressure diffusion*

At present, we do not make *in situ* pressure measurements in the turbulence facility, nor do we have measurements with sufficient temporal resolution to allow for the direct computation of pressure gradients from PIV data using methods such as those shown by Dabiri *et al.* (2014). However, by considering the turbulent kinetic energy balance and computing pressure diffusion as the residual, it is apparent that pressure plays a significant role at the bed to balance non-zero dissipation, since all other terms approach zero at the bed. In particular, the bed-normal component $p_z = -(1/\rho_0)(\partial \overline{w'p'}/\partial z)$ would likely be of greatest significance, and it is something that we will revisit in future experiments to evaluate its role in the energy balance.

Figure 16 shows typical relative contributions of production and dissipation (and the remaining terms in the energy balance) for the case of near-zero production. The relative magnitude of the pressure term is significant within the buffer layer. Due to this increase, we hypothesize that significant pressure fluctuations in the boundary layer contribute to the increase in k observed in figures 5 and 6 in the absence of an active source of turbulent kinetic energy near the stationary solid bed.

5.5. *Turbulence metrics*

Having completed analysis of many higher-order turbulence statistics, we can compute traditional metrics of the flow such as Kolmogorov scales, Taylor scales, Reynolds numbers and others. The quantities included are all computed in the mixed region of the flow. Using the estimate for integral length scale found via the exponential fit to the longitudinal autocorrelation function and the dissipation rate calculated directly, we compute the Kolmogorov time scale, $\tau = (\nu/\epsilon)^{1/2}$, which ranges from 0.023 to 0.034 s with the 8 × 8 RASJA. Values of the Kolmogorov length scale, $\eta \equiv (\nu^3/\epsilon)^{1/4}$, range from 0.016 to 0.019 cm within the 8 × 8 RASJA. Within the 16 × 16 RASJA, values of τ range from 0.017 to 0.025 s, and values of η range from 0.013 to 0.016 cm. It appears that both τ and η decrease with increasing T_{on}, as shown by the sample statistics in tables 7 and 8, consistent with expectations given that turbulent kinetic energy increases with T_{on}.

Φ_{on} (%)	T_{on} (s)	τ (s)	η (cm)	λ (cm)
6.25	4	0.035	0.019	0.42
6.25	6	0.032	0.018	0.42
6.25	8	0.029	0.017	0.45

TABLE 7. Kolmogorov and Taylor scales, 8×8 RASJA.

Φ_{on} (%)	T_{on} (s)	τ (s)	η (cm)	λ (cm)
3.1	0.8	0.025	0.016	0.33
3.1	1.0	0.022	0.015	0.33
3.1	1.2	0.019	0.014	0.30
3.1	1.4	0.018	0.014	0.30
3.1	1.6	0.017	0.013	0.29

TABLE 8. Kolmogorov and Taylor scales, 16×16 RASJA.

We also compute the Taylor microscale, $\lambda_g = \sqrt{10}\eta^{2/3}\mathcal{L}^{1/3}$, which gives us an intermediate length scale of the turbulence. In the 8×8 RASJA, λ_g ranges from 0.40 to 0.45 cm across all 15 cases. In the 16×16 RASJA, λ_g ranges from 0.29 to 0.33 cm, with no clear dependence of T_{on} on λ_g. The Reynolds number based on the Taylor microscale, $Re_\lambda = ((2/3)k)\sqrt{15/\nu\epsilon}$, in which we use the average k from the mixed region of the flow, provides a traditional metric of grid turbulence. Across all 15 trials with the 8×8 RASJA, our values range from 277 to 378, as shown in table 9, consistent with results in Variano & Cowen (2008). Using the 16×16 RASJA, Re_λ ranges from 197 to 262, shown in table 10.

We compute a grid Reynolds number, $Re_G = 2(\sqrt{(2/3)k}\mathcal{L}/\nu)$, for comparison to prior experiments in GSTs, and $Re_L = Re^* = k^2/\epsilon\nu$ for comparison to moving-bed experiments. These Reynolds numbers show highly turbulent flow, with values greater than much of the prior literature in this field, such as Brumley & Jirka (1987) with $Re_\lambda = 74$, $Re_L = 390$, Uzkan & Reynolds (1967) with $Re_L = 90$, Thomas & Hancock (1977) with $Re_L = 2000$, and Perot & Moin (1995*a*) with Re_L ranging from 6.2 to 374.

From the Reynolds number, we can approximate a viscous sublayer thickness, $\delta_\nu \approx 2\mathcal{L}_L Re_L^{-1/2}$, from scaling arguments as in Brumley & Jirka (1987), Calmet & Magnaudet (2003) and Variano & Cowen (2008). For all 15 of the cases considered with the 8×8 RASJA, we consistently obtain a value of $\delta_\nu \approx 0.24 \pm 0.01$ cm. This is very close to the value of 0.26 cm determined by Variano & Cowen (2008). It includes one data point given the spatial resolution of 0.176 cm used in our PIV measurements. Thus, this prevents us from measuring velocity gradients within the viscous sublayer. With the 16×16 RASJA, $\delta_\nu \approx 0.11 \pm 0.01$ cm, which is too thin to measure with our current experimental set-up. Upon determining δ_ν, we can also consider the relationship $w'^2 = \beta\epsilon^{2/3}(z + \delta_\nu)^{2/3}$ as presented in Hunt (1984), Calmet & Magnaudet (2003) and Variano & Cowen (2008). Given the substantial increase in ϵ as z approaches zero, we use ϵ_m and find the relationship to hold for approximately $10\delta_\nu < z < 0.7\mathcal{L}$, with $\beta = 1.75 \pm 0.23$ across the 15 cases with the 8×8 RASJA. Although we find a wide range of β, this is near the theoretical prediction of $\beta \approx 1.8$ (Hunt 1984) and experimental results $\beta \approx 2.0$ (Calmet & Magnaudet 2003) and $\beta \approx 1.5$ (Variano & Cowen 2008).

Φ_{on} (%)	T_{on} (s)	Re_λ	Re_G	$Re_L = Re^*$	$\kappa_t \left(\frac{\text{cm}^2}{\text{s}}\right)$	Pe
6.25	4	288	6 310	12 500	38.63	0.021
6.25	6	334	7 800	16 800	47.76	0.010
6.25	8	378	11 400	21 500	69.72	0.046

TABLE 9. Reynolds numbers and Péclet number, 8×8 RASJA.

Φ_{on} (%)	T_{on} (s)	Re_λ	Re_G	$Re_L = Re^*$	$\kappa_t \left(\frac{\text{cm}^2}{\text{s}}\right)$	Pe
3.1	0.8	197	4 200	5 810	25.72	0.055
3.1	1.0	218	5 212	7 160	31.92	0.035
3.1	1.2	230	5 172	7 910	31.67	0.018
3.1	1.4	249	5 370	9 340	32.89	0.002
3.1	1.6	262	6 000	10 300	36.74	0.025

TABLE 10. Reynolds numbers and Péclet number, 16×16 RASJA.

The Péclet number, in general, defines the ratio of advective transport to diffusive transport – large Péclet number indicates that advection dominates while small indicates that diffusion dominates. In this set-up we use a simple scaling analysis to define a Péclet number. We represent the time scale of the advective processes as the integral length scale of the turbulence divided by the mean velocity or $\tau_{adv} = \mathcal{L}/\overline{U}$. We represent the time scale of the turbulent diffusive processes as $\tau_{diff} = \mathcal{L}^2/\kappa_t$ where $\kappa_t = \sqrt{k}\mathcal{L}$ and hence $\tau_{diff} = \mathcal{L}/\sqrt{k}$. Thus, in our facility, we use Péclet number $= Pe = \overline{U}/\sqrt{k}$, which is the inverse of the turbulence intensity, as a measure of the relative importance of turbulent stirring to advection by the mean flow. Values of less than 0.1 confirm the highly diffusive nature of the facility in which turbulent transport overwhelms advective transport. The aforementioned statistics are summarized in tables 9 and 10.

6. Discussion

6.1. *Turbulent velocities and turbulent kinetic energy*

The following are comparisons between our experimental results with the moving-bed experiment of Thomas & Hancock (1977) and RDT of Hunt & Graham (1978) and Hunt (1984) for both inviscid and viscous cases. The turbulence generating mechanisms and imposed boundary conditions are very different between our experiments and the moving-bed studies so we do not expect complete agreement. Furthermore, the results presented in Thomas & Hancock (1977) and Hunt & Graham (1978) are spatially dependent, which provides an additional layer of complexity.

We show two sets of results in the moving-bed experiments: $x/J = 13$ and $x/J = 25$, where the ratio of downstream distance x to grid spacing J gives a measure of the relative development of the turbulent boundary layer as it decays along the moving bed. We do not include the moving-bed data of Uzkan & Reynolds (1967) due to the low magnitude of the integral length scale reported that consequently alters the scaling significantly so as not to produce comparable results, as is argued in Thomas & Hancock (1977).

Figure 17 shows the inviscid RDT profiles for turbulent velocities, including both linear theory of Hunt & Graham (1978) and the nonlinear correction of Hunt (1984).

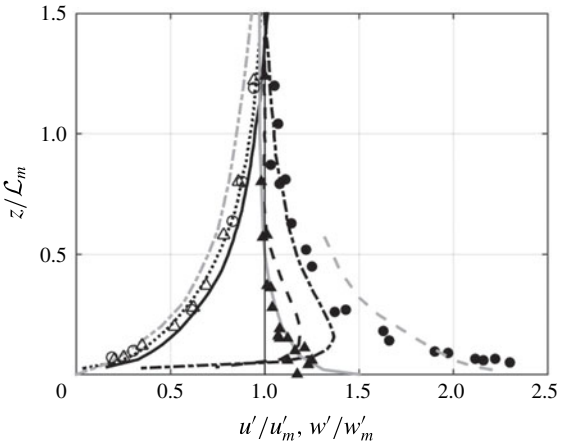

FIGURE 17. Comparison of u'/u'_m, w'/w'_m with Hunt & Graham (1978) inviscid theory ($u'/u'_m(-)$ (grey), $w'/w'_m(-\cdot)$ grey) with nonlinear correction (– grey) of Hunt (1984) and Thomas & Hancock (1977) experimental moving-bed data at $x/J = 25$ (●), $x/J = 13$ (▲). Present cases are for $\Phi_{on} = 6.25\,\%$ and $T_{on} = 4$ s ($u'/u'_m - \cdot$, $w'/w'_m \cdots$), 8×8 RASJA, $\Phi_{on} = 3.1\,\%$ and $T_{on} = 0.8$ s ($u'/u'_m - -$, $w'/w'_m -$), 16×16 RASJA.

We include one experimental trial from each RASJA. Our bed-normal r.m.s. velocity trials collapse and scale well with the moving bed experiments and theory. However, the wall-parallel r.m.s. velocity proves more complicated.

Away from the wall ($z/L_m > 0.1$), the inviscid theory qualitatively serves well. In the case of the moving-bed experiments, this normalization is limited by its ability to properly scale with downstream turbulence development, as is evident by the agreement observed with the $x/J = 13$ moving-bed data, whereas at $x/J = 25$, u'/u'_m shows a greater departure from unity away from the wall. Quantitatively, although the present experimental trials within each facility collapse well (shown in greater detail in Johnson 2016), the representative trials from each the 8×8 and 16×16 RASJAs do not identically collapse with each other. Despite similar magnitudes of Re_λ and k between the cases selected, we attribute this discrepancy to the notably different H/J ratios between the two facilities. We also find the experimental cases do not align precisely with data from theory or moving-bed experiments. While the enhancement in u' in the present experimental data is not as great as the amplification shown in Hunt (1984) or in the developed $x/J = 25$ trial of Thomas & Hancock (1977), it is also more significant than the increase in u' suggested by linear theory of Hunt & Graham (1978) or relatively weakly developed boundary layer in the $x/J = 13$ case.

Close to the wall ($z/L_m < 0.1$), the viscous model of Hunt & Graham (1978) shown in figure 18 better captures the wall-parallel velocity fluctuations that decay to zero at the bed. The moving-bed experimental data do not follow this trend, likely due to their inability to measure within the viscous boundary layer (Thomas & Hancock 1977).

We find a similar disparity when considering the inviscid model for k near the wall, shown in figure 19. Due to the no-slip boundary condition, k approaches zero at $z = 0$ whereas inviscid RDT suggests $k/k_m = 1$ at the moving bed. Furthermore, rather than k decaying gradually with increasing depth, we experimentally observe $k/k_m > 1$ near the bed with a peak near $z/\mathcal{L}_m = 0.1$, as discussed previously.

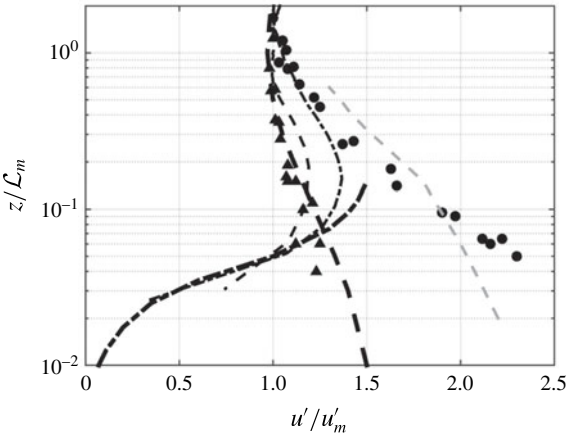

FIGURE 18. Viscous (−·) and source (−−) regions of u'/u'_m. See previous figure for legend.

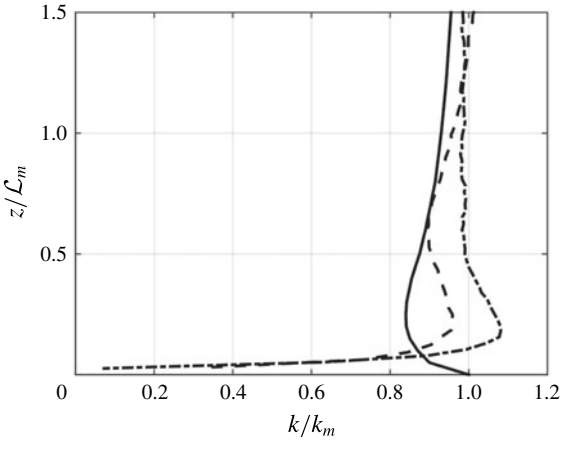

FIGURE 19. Comparison of k/k_m with Hunt & Graham (1978) inviscid theory (−). Present cases are for $\Phi_{on} = 6.25\,\%$ and $T_{on} = 4$ s $(k/k_m - \cdot)$, 8×8 RASJA, $\Phi_{on} = 3.1\,\%$ and $T_{on} = 0.8$ s $(k/k_m - -)$, 16×16 RASJA.

We can also consider the spatial autocorrelation coefficient (referred to as a cross-correlation in Hunt 1984) of vertical velocity. Near the boundary, Hunt (1984) approximates

$$\frac{\overline{w(z_1)w(z)}}{\overline{w^2(z_1)}} \approx \frac{z}{z_1} \tag{6.1}$$

to describe the normalized autocorrelation near the boundary between two points separated by a vertical distance $|z_1 - z|$. We compute the normalized autocorrelation at $z_1 = \mathcal{L}$ and $z_1 = 0.3\mathcal{L}$, as shown in figure 20. The present experimental data show a significant departure from the theory of Hunt (1984), with high correlation in the source and buffer regions then rapid decay to zero in the viscous region, in contrast to the predicted linear decay of the autocorrelation with z via RDT.

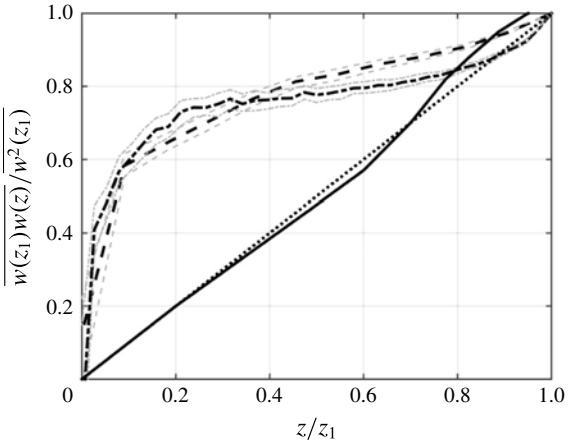

FIGURE 20. Normalized spatial autocorrelation of vertical velocity comparison with Hunt (1984) theory (−) and z/z_1 approximation (···). Present data shown with 95 % confidence intervals for $z_1 = \mathcal{L}$ (−·) and $z_1 = 0.3\mathcal{L}$ (−−), $\Phi_{on} = 6.25\,\%$ and $T_{on} = 4$ s, 8×8 RASJA.

Whereas there are boundary layer data that support the theoretical linear relationship of Hunt (1984), we compute values of *Pe* from the field data of Hunt, Kaimal & Gaynor (1988) ranging from 4.6 to 22.9, whereas *Pe* values in the present experiments are well below unity, as shown in tables 9 and 10. Although it is noted that among experiments in prior literature, additional shear does not significantly alter the linear autocorrelation (Hunt *et al.* 1988), the flow conditions have baseline mean shear that is absent from our turbulence experiments, which could explain the behavioural difference. It would be valuable to vary *Pe* across the range of all experiments and test whether this explains the difference in the behaviour of the spatial autocorrelation.

6.2. *Integral length scale*

Further evidence of the physical nature of turbulent splats and the significant intercomponent energy transfer in the buffer region is shown when we reconsider the integral length scale. A scaling of figure 9 better highlights the stretching of horizontal motions observed within one integral length scale of the bed. Figure 21 shows that whereas Hunt & Graham (1978) find a 5 % increase in $\mathcal{L}_L$ near $z/\mathcal{L}_L = 1$, and Thomas & Hancock (1977) find nearly a 10 % increase near $(z/\mathcal{L}_L) = 0.5$, our data show 25–40 % increases in the length scale of bed-parallel motions. The significant enhancement in $\mathcal{L}_L$ in the present experiments further highlights the energetic bed-parallel motions that contribute to the increase in k observed in the buffer region. At $z = 0$, RDT suggests $\mathcal{L}_L/\mathcal{L}_{L,m} = 2/3$ (Thomas & Hancock 1977), which is a reasonable estimate if our data were extrapolated further. The transverse integral length scale profiles in figure 21 align well and approach zero at the bed, as is consistent with theory.

6.3. *Dissipation*

Teixeira & Belcher (2000) extended the RDT work of Hunt & Graham (1978) to account for dissipation. With strict assumptions of isotropy, they only consider diagonal components of Reynolds stress and dissipation terms. Thus, component-based

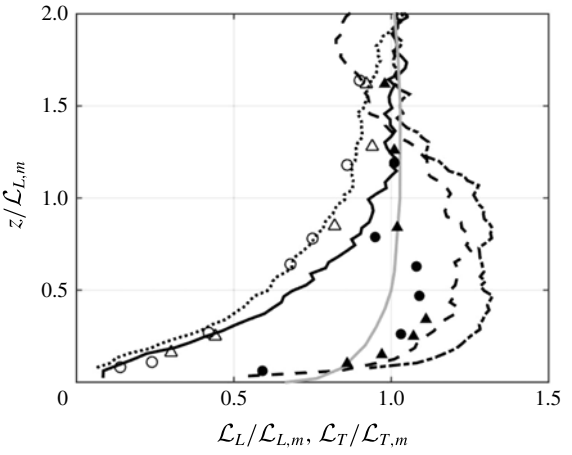

FIGURE 21. Longitudinal and transverse integral length scale comparison with Hunt & Graham (1978) theory (− grey) and Thomas & Hancock (1977). See figure 17 for legend.

dissipation simplifies to $\epsilon_{11} = 2\nu[2\overline{(\partial u/\partial x)^2} + \overline{(\partial u/\partial z)^2}]$ and $\epsilon_{33} = 2\nu[2\overline{(\partial w/\partial x)^2} + \overline{(\partial w/\partial z)^2}]$. We assume radial symmetry so that $\epsilon_{22} = \epsilon_{11}$. We draw comparisons between these contributions in figures 22 and 23. It is important to note that our experiments are performed at much greater Reynolds numbers than these simulations; using $Re^* = k^2/\nu\epsilon$, we find experimental values of order 10 000, whereas Teixeira & Belcher (2000) and Perot & Moin (1995*b*) have values of Re^* of 134 in the cases considered.

As both the theoretical work of Teixeira & Belcher (2000) and DNS studies of Perot & Moin (1995*b*) address developing turbulent boundaries layers, we explore how our stationary data compare with their evolving profiles. At the initial insertion of the wall in RDT, our data and the DNS data show distinct disagreements at the bed for both the $\epsilon_{11}/\epsilon_{11,m}$ and $\epsilon_{33}/\epsilon_{33,m}$ cases, as one would expect.

At later times, the no-slip boundary develops and $\epsilon_{33}/\epsilon_{33,m}$ approaches zero; the intercomponent energy transfer becomes more evident as $\epsilon_{11}/\epsilon_{11,m}$ increases at the bed. The wall-parallel dissipation component shows excellent agreement between our experimental data and the DNS data at $\sqrt{k}t/\mathcal{L}^* = 2.0$, and with RDT at $\sqrt{k}t/\mathcal{L}^* = 0.10$, though one can imagine an extrapolation of the $\epsilon_{11}/\epsilon_{11,m}$ data with the 16×16 RASJA would reach a lower magnitude at the bed. In the bed-normal component, our experimental ϵ_{33} with the 8×8 RASJA approaches the mixed value more rapidly than the DNS or RDT at $\sqrt{k}t/\mathcal{L}^* = 0.10$; however, $\epsilon_{33}/\epsilon_{33,m}$ does not reach unity until $z/\mathcal{L} > 1.5$. Similarly, the $\epsilon_{33}/\epsilon_{33,m}$ data with the 16×16 RASJA do not reach unity until $z/\mathcal{L} > 1.5$, beyond the scope of this comparison.

Total dissipation, $\epsilon_{TB} = (1/2)(\epsilon_{11} + \epsilon_{22} + \epsilon_{33})$, expands to

$$\epsilon_{TB} = \nu\left[4\overline{\left(\frac{\partial u}{\partial x}\right)^2} + 2\overline{\left(\frac{\partial u}{\partial z}\right)^2} + 2\overline{\left(\frac{\partial w}{\partial x}\right)^2} + \overline{\left(\frac{\partial w}{\partial z}\right)^2}\right] \tag{6.2}$$

by applying radial symmetry to the Teixeira & Belcher (2000) formulation. This equation describes pseudo-dissipation, and it shows several obvious differences between our direct method of computing actual dissipation, which did not assume

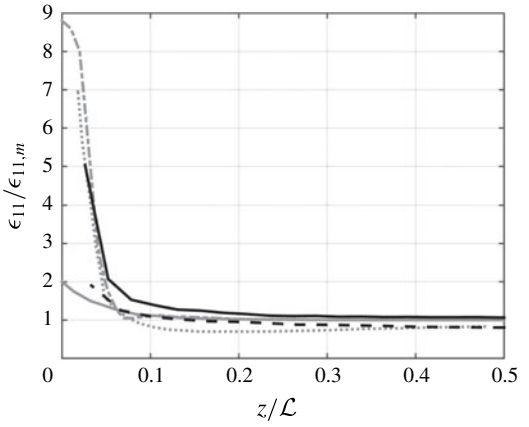

FIGURE 22. ϵ_{11} comparison to Teixeira & Belcher (2000) (– (grey) – $\sqrt{kt}/\mathcal{L}^* = 0$, inviscid theory; (–· (grey) – $\sqrt{kt}/\mathcal{L}^* = 0.10$, viscous theory, $Re^* = 134$); Perot & Moin (1995*b*) (··· (grey) $-\sqrt{kt}/\mathcal{L}^* = 2.0$, $Re^* = 134$). Present cases for $\Phi_{on} = 6.25\,\%$, $T_{on} = 4$ s (–), $Re^* = 12\,500$, 8×8 RASJA. $\Phi_{on} = 3.1\,\%$, $T_{on} = 0.8$ s (––), $Re^* = 5800$, 16×16 RASJA.

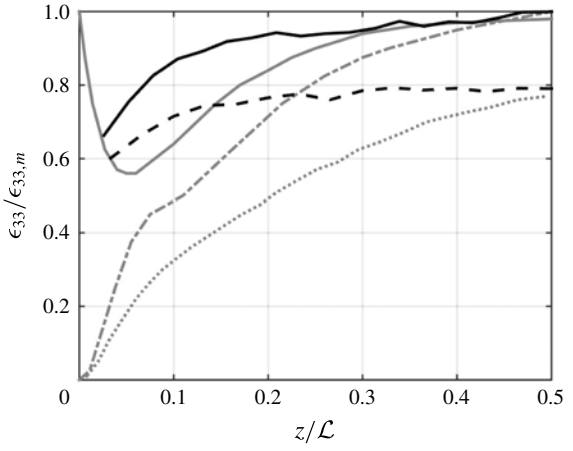

FIGURE 23. ϵ_{33} comparison. See previous figure for legend.

strict isotropy, but only radial symmetry. This theoretical method underestimates our results by approximately 44 %, due primarily to the altered coefficients of the diagonal terms of the stress tensor.

By contrast, Teixeira & da Silva (2012) compute the full dissipation rate as

$$\epsilon_{TdS} = 2\nu\left[4\overline{\left(\frac{\partial u}{\partial x}\right)^2} + \overline{\left(\frac{\partial u}{\partial z}\right)^2} + \overline{\left(\frac{\partial w}{\partial x}\right)^2} + \overline{\left(\frac{\partial w}{\partial z}\right)^2} + 2\overline{\left(\frac{\partial u}{\partial z}\frac{\partial w}{\partial x}\right)}\right], \tag{6.3}$$

which improves agreement with our direct dissipation calculations to account for 87 % of the total dissipation. Furthermore, Teixeira & da Silva (2012) consider the increase in dissipation at the bed, finding a peak $\epsilon(z = 0) = (17/15)\epsilon_m$. By applying

our direct method formulation and the Teixeira & da Silva (2012) formulation, we find significantly larger ratios of bed dissipation to mixed dissipation ranging from 1.5 to 3.6 across the experimental cases considered.

7. Conclusions

The facility we developed generates high Reynolds number turbulence that is horizontally homogeneous and nearly isotropic in the mixed region with consistently negligible secondary mean flows. We see strong intercomponent energy transfer and evidence of turbulent splats near the bed, characterized by the transition from w' to u' and loss of isotropy, with strong local shear and likely significant instantaneous pressure gradients generating an increase in k near the bed. We are able to control the relative magnitudes of turbulent statistics such as u', w', k, ϵ and, importantly, $\mathcal{L}$, by altering the mean on-time in the jet-firing algorithm, and we are the first to show the ability to vary $\mathcal{L}$ in this type of facility by changing the jet-firing algorithm.

The results we obtain have several distinct differences from prior facilities and theories designed to study turbulence in a mean shear free environment. The data in the moving-bed studies of Thomas & Hancock (1977) and Hunt & Graham (1978) show agreement with our results in the inviscid models when the flow is greater than one integral length scale above the bed. However, these models and experiments do not show as energetic a boundary as we find in our experiments, or as the nonlinear theory of Hunt (1984) suggests, in particular for $(z/\mathcal{L}) < 0.5$. It appears the moving bed may be dampening potential splats, due to the discrepancies observed in turbulent kinetic energy and integral length scale profiles. This could also be a result of the significantly lower Reynolds numbers in the moving-bed simulations than in our experimental facility.

Furthermore, because the aforementioned studies, in addition to RDT and DNS studies of Teixeira & Belcher (2000) and Perot & Moin (1995*b*), respectively, are time dependent, it appears that our data more closely align with these studies at later time scales, when the forced turbulent flow has had time to respond to the presence of the solid boundary. This is indeed a quick transition, as is observed in figures 22 and 23, though the lack of collapse in figure 18 suggests that these models are limited in capturing fully developed turbulent boundaries.

When exploring the turbulent kinetic energy balance, we find that we are able to calculate dissipation directly from our PIV data as our velocity field is sufficiently resolved. With our estimate of dissipation, we provide additional estimates of the coefficients needed to compute dissipation via Eulerian frequency spectra, when low mean flows prevent the use of Taylor's frozen turbulence hypothesis for temporal measurements of turbulent flows.

We see that dissipation, turbulent transport, and pressure play the greatest roles in the mean shear free turbulent boundary layer generated from homogeneous isotropic turbulence. Despite such weak mean shear, we know that there are highly energetic local shear events at the bed, due to turbulent splats and intercomponent energy transfer, that make this type of facility and boundary layer of unique importance.

Acknowledgements

The authors greatly appreciate the financial support provided by the Division of Chemical, Bioengineering, Environmental, and Transport Systems of the US National Science Foundation (Award no. 1233842). We also wish to thank P. Charles for his work in maintaining and improving the experimental facility and F. Guimbretière

for his assistance in developing the Arduino-MATLAB interface. Undergraduate students Z. Shiveley, B. Powell and C. DeVoe assisted with RASJA construction, data collection and maintenance of optimal jet performance. E. Variano entertained with many enlightening discussions about turbulence and the joys and struggles of working with random jet arrays. Finally, we graciously acknowledge the editor and anonymous reviewers for their thoughtful contributions.

REFERENCES

BRUMLEY, B. H. & JIRKA, G. H. 1987 Near-surface turbulence in a grid-stirred tank. *J. Fluid Mech.* **183**, 235–263.

CALMET, I. & MAGNAUDET, J. 2003 Statistical structure of high-Reynolds-number turbulence close to the free surface of an open-channel flow. *J. Fluid Mech.* **474**, 355–378.

COWEN, E. A. & MONISMITH, S. G. 1997 A hybrid digital particle tracking velocimetry technique. *Exp. Fluids* **22**, 199–211.

COWEN, E. A., SOU, I. M., LIU, P. L. & RAUBENHEIMER, B. 2003 Particle image velocimetry measurements within a laboratory-generated swash zone. *J. Engng Mech. ASCE* **129** (10), 1119–1129.

DABIRI, J. O., BOSE, S., GEMMELI, B., COLIN, S. P. & COSTELLO, J. H. 2014 An algorithm to estimate unsteady and quasi-steady pressure fields from velocity field measurements. *J. Expl Biol.* **217**, 331–336.

DE SILVA, I. P. D. & FERNANDO, H. J. S. 1994 Oscillating grids as a source of nearly isotropic turbulence. *Phys. Fluids* **6**, 2455–2464.

DORON, P., BERTUCCIOLI, L., KATZ, J. & OSBORN, T. R. 2000 Turbulence characteristics and dissipation estimates in the coastal ocean bottom boundary layer from PIV data. *J. Phys. Oceanogr.* **31**, 2108–2134.

EFRON, B. & TIBSHIRANI, R. 1993 *An Introduction to the Bootstrap*. Chapman & Hall.

HERLINA, H. & WISSINK, J. G. 2016 Isotropic-turbulence-induced mass transfer across a severely contaminated water surface. *J. Fluid Mech.* **797**, 665–682.

HOPFINGER, E. J. & TOLY, J.-A. 1976 Spatially decaying turbulence and its relation to mixing across density interfaces. *J. Fluid Mech.* **78** (1), 155–175.

HUNT, J. C. R. 1984 Turbulence structure in thermal convection and shear-free boundary layers. *J. Fluid Mech.* **138**, 161–184.

HUNT, J. C. R., KAIMAL, J. C. & GAYNOR, J. E. 1988 Eddy structure in the convective boundary layer: new measurements and new concepts. *Q. J. R. Meteorol. Soc.* **114** (482), 827–858.

HUNT, J. & GRAHAM, J. 1978 Free-stream turbulence near plane boundaries. *J. Fluid Mech.* **84**, 209–235.

JOHNSON, B. A. 2016 Turbulent boundary layers and sediment suspension absent mean flow-induced shear. PhD thesis, Cornell University.

KHAKPOUR, H. R., SHEN, L. & YUE, D. K. P. 2011 Transport of passive scalar in turbulent shear flow under a clean or surfactant-contaminated free surface. *J. Fluid Mech.* **670**, 527–557.

KIT, E., FERNANDO, J. S. & BROWN, J. A. 1995 Experimental examination of Eulerian frequency spectra in zero-mean-shear turbulence. *Phys. Fluids* **7**, 1168–1170.

LIAO, Q. & COWEN, E. A. 2005 An efficient anti-aliasing spectral continuous window shifting technique for PIV. *Exp. Fluids* **38**, 197–208.

MAKITA, H. 1991 Realization of a large-scale turbulence field in a small wind tunnel. *Fluid Dyn. Res.* **8**, 53–64.

MCDOUGALL, T. 1979 Measurements of turbulence in a zero-mean-shear mixed layer. *J. Fluid Mech.* **94** (3), 409–431.

MCKENNA, S. P. & MCGILLIS, W. R. 2004 Observations of flow repeatability and secondary circulation in an osillating grid-stirred tank. *Phys. Fluids* **16** (9), 3499–3502.

MYDLARSKI, L. & WARHAFT, Z. 1996 On the onset of high-Reynolds-number grid-generated wind tunnel turbulence. *J. Fluid Mech.* **320**, 331–368.

PAO, Y.-H. 1965 Structure of turbulent velocity and scalar fields at large wavenumbers. *Phys. Fluids* **8** (6), 1063–1075.

PEREZ-ALVARADO, A., MYDLARSKI, L. & GASKIN, S. 2016 Effect of the driving algorithm on the turbulence generated by a random jet array. *Exp. Fluids* **57** (2), 20.

PEROT, B. & MOIN, P. 1995*a* Shear-free turbulent boundary layers. Part 1. Physical insights into near-wall turbulence. *J. Fluid Mech.* **295**, 199–227.

PEROT, B. & MOIN, P. 1995*b* Shear-free turbulent boundary layers. Part 2. New concepts for Reynolds stress transport equation modelling of inhomogeneous flows. *J. Fluid Mech.* **295**, 229–245.

PETERS, N. 1999 The turbulent burning velocity for large-scale and small-scale turbulence. *J. Fluid Mech.* **384**, 107–132.

POPE, S. B. 2000 *Turbulent Flows*. Cambridge University Press.

ROUSE, H. & DODU, J. 1955 Diffusion turbulente à travers une discontinuité de densité. *La Houille Blanche* **10**, 522–532.

SHEN, L., YUE, D. K. P. & TRIANTAFYLLOU, G. S. 2004 Effect of surfactants on free-surface turbulent flows. *J. Fluid Mech.* **506**, 79–115.

SPALART, P. R. 1988 Direct simulation of a turbulent boundary layer up to $r = 1410$. *J. Fluid Mech.* **187**, 61–98.

TEIXEIRA, M. A. C. & BELCHER, S. E. 2000 Dissipation of shear-free turbulence near boundaries. *J. Fluid Mech.* **422**, 167–191.

TEIXEIRA, M. A. C. & DA SILVA, C. B. 2012 Turbulence dynamics near a turbulent/non-turbulent interface. *J. Fluid Mech.* **695**, 257–287.

TENNEKES, H. 1975 Eulerian and Lagrangian time microscales in isotropic turbulence. *J. Fluid Mech.* **67**, 561–567.

THOMAS, N. H. & HANCOCK, P. E. 1977 Grid turbulence near a moving wall. *J. Fluid Mech.* **82**, 481–496.

THOMPSON, S. M. & TURNER, J. S. 1975 Mixing across an interface due to turbulence generated by an oscillating grid. *J. Fluid Mech.* **67** (2), 349–368.

UZKAN, T. & REYNOLDS, W. C. 1967 A shear-free turbulent boundary layer. *J. Fluid Mech.* **28**, 803–821.

VARIANO, E. A. 2007 Measurements of gas transfer and turbulence at a shear-free turbulent air-water interface. PhD thesis, Cornell University.

VARIANO, E. A., BODENSCHATZ, E. & COWEN, E. A. 2004 A random synthetic jet array driven turbulence tank. *Exp. Fluids* **37**, 613–615.

VARIANO, E. A. & COWEN, E. A. 2008 A random-jet-stirred turbulence tank. *J. Fluid Mech.* **604**, 1–32.

VARIANO, E. A. & COWEN, E. A. 2013 Turbulent transport of a high-Schmidt-number scalar near an air-water interface. *J. Fluid Mech.* **731**, 259–287.

VON KÁRMÁN, T. 1930 Mechanische Ähnlichkeit und Turbulenz. *Nachrichten von der Gesellschaft der Wissenschaften zu Goettingen* **5**, 58–76.

WESTERWEEL, J. 1994 Efficient detection of spurious vectors in particle image velocimetry data. *Exp. Fluids* **16**, 236–247.